
Enhancing Collection Efficiency of
Nitrogen Vacancy Center Fluorescence in Diamond
Using a Solid Immersion Lens

Master Thesis in Nanoscience, University of Basel

Dominik Rohner

November 21, 2013



Submitted to:

Prof. Patrick Maletinsky and Prof. Richard Warburton

Department of Physics

University of Basel, Switzerland

dominik.rohner@stud.unibas.ch

Abstract

Negatively charged nitrogen vacancy (NV) centers in diamond are of great interest in quantum information science due to their long spin coherence times at room temperature. However, only a small amount of its fluorescence can usually be collected because of the high refractive index of diamond ($n = 2.4$). In this work, the collection efficiency of NV center fluorescence was increased using solid immersion lenses.

The saturation count rate of a single NV center in bulk diamond was measured to be 75 ± 2 kcps without and 325 ± 3 kcps with a ZrO_2 solid immersion lens (SIL). This represents an increase by a factor of 4.3 in collection efficiency which is relatively close to the theoretically expected factor of 5.8. Additionally, a resolution enhancement of roughly factor $n_{\text{ZrO}_2} = 2.2$ was found. No increase of the count rate was observed using a GaP SIL on bulk diamond, supposedly due to a remaining air gap between diamond and SIL.

To create a dielectric antenna which should allow for near-unity collection efficiency, $1.5 \mu\text{m}$ thick pieces of diamond containing NV centers were transferred to a GaP SIL. A significant difference in count rates between well and less well contacted pieces was found, demonstrating at least a partial functionality of the dielectric antenna. Back focal plane images showing the angle of the collected light confirmed the different contact qualities of the thin diamond pieces in terms of emission angles. However, no single NV centers could be observed here and the absolute count rates were lower than what would be expected for a well functioning dielectric antenna. These problems will be addressed by using cleaner diamond membranes and making further investigations.

Contents

1	Introduction	1
2	Theory	3
2.1	The NV Center	3
2.2	Solid Immersion Lens	6
2.3	Dielectric Antenna	9
2.4	Back Focal Plane Imaging	10
3	Materials and Methods	12
3.1	Confocal Microscope	12
3.2	Back Focal Plane Imaging Setup	13
3.3	SILs	14
4	Results and Discussion	16
4.1	ZrO ₂ SIL	16
4.1.1	Resolution Measurement	16
4.1.2	ZrO ₂ SIL on Bulk Diamond	17
4.2	GaP SIL	20
4.2.1	Resolution Measurement	20
4.2.2	GaP SIL on Bulk Diamond	22
4.3	Thin Diamond Slabs and Cantilevers	25
4.3.1	ZrO ₂ SIL	25
4.3.2	GaP SIL	27
4.4	Back Focal Plane Imaging	31
5	Summary and Outlook	36
	References	41
	Appendix	42

1 Introduction

The nitrogen-vacancy (NV) center in diamond has been studied since the 1970s [1] and gained renewed interest since the detection of single NV centers in a confocal microscope in 1997 [2]. Its electron spin can be initialized and read out optically and has a long coherence time even at room temperature (up to 2 ms [3]), rendering the NV center a highly interesting candidate for a solid-state spin-qubit in quantum information technology [4]. Additionally, the NV center can be used for high-resolution magnetometry [5][6] and other metrology applications [7].

However, a significant challenge concerning the NV center is that it is located in diamond, a material with a high refractive index ($n = 2.4$). Therefore, only about 2% to 3% of its fluorescence is collected with regular optics ($NA = 0.8$) due to refraction and total internal reflection at the diamond-air interface. A better collection efficiency and therefore a higher signal-to-noise ratio is critical for many applications. In quantum cryptography, where triggered single photons are used to encrypt and transmit information, the collection efficiency is the main limiting factor of the secure bit rate [8]. In magnetometry, the magnetic field sensitivity scales with the square root of the count rate [9]. However, the collection efficiency is even more critical when two-photon processes with NV centers are targeted, such as in two-photon interferometry [10] or remote entanglement [11], leading to a quadratic dependency of the signal on the count rate.

So far, various promising methods have been suggested to facilitate the light out-coupling from diamond and therefore increase the collection efficiency. On the one hand, this can be done by structuring diamond, e.g. in the case of free-standing diamond nanowires produced by nanofabrication techniques. Almost an order of magnitude higher collection efficiencies from NV centers located inside such nanowires have been demonstrated [12]. Nanodiamonds also yield higher collection efficiencies than bulk diamond because their subwavelength size renders refraction irrelevant [13]. However, interaction with the near surfaces and strain fields often decrease coherence times and optical stability of NV centers in these materials [14]. On the other hand, the use of a high-index solid immersion lens (SIL) on top of the diamond sample is an alternative method to increase the collection efficiency significantly while maintaining the advantageous properties of the NV centers [15]. Possible materials for a SIL are zirconia ($n_{ZrO_2} = 2.2$) or gallium phosphide ($n_{GaP} = 3.3$). Interesting approaches are also to etch arrays of microscopic SILs directly into the diamond surface using focused ion beam (FIB) [16] or to fabricate macroscopic

diamond SILs [17].

Nevertheless, even with an ideal SIL or nanowire, at most half of the fluorescence is directed into the half-space which can be collected by the objective. To overcome this limitation, a dielectric antenna was recently proposed where the emitter is located in a dielectric layer between a higher- and a lower-index medium [18]. In this case, most of the light is guided into the high-index material, directing it towards the collection optics and allowing for near-unity collection efficiencies [19]. In such dielectric antennas, the emission characteristically peaks around the critical angle in the high-index medium which can be measured by the angle-resolving back focal plane imaging [20]. Since the refractive index of diamond is already high, the creation of a dielectric antenna is challenging due to the need for SIL with a significantly higher index. GaP with its index of 3.3 and transparency in the spectral range of the NV center fluorescence appears to be the only material suited for this purpose.

This master thesis first presents the necessary theoretical background of the NV center, SILs, the dielectric antenna and back focal plane imaging in Chap. 2. Chap. 3 describes the experimental setup and the used methods. The main part of the thesis is Chap. 4 which contains the experimental results and their discussion. It includes collection efficiency measurements with ZrO₂ and GaP SILs on bulk diamond, experiments towards the realization of a dielectric antenna for NV centers and angle-resolved detection through back focal plane imaging. Finally, a conclusion and an outlook on future experiments are given in Chap. 5.

2 Theory

2.1 The NV Center

The NV center in diamond is a defect where two neighbouring carbon atoms are substituted by a nitrogen atom and a vacancy, resulting in a defect with C_{3v} symmetry with the high symmetry axis along the N-V connection line (Fig. 1 a). The three dangling carbon bonds, the two lone pair electrons from the nitrogen plus one extra electron make a total of 6 electrons in the negatively charged NV^- center [21].¹ The electronic structure of the NV center is depicted in Fig. 1 b). The ground state consists of a spin triplet with $m_s = 0$ and $m_s = \pm 1$ states, where m_s denotes the spin projection on the NV axis. At zero magnetic field, $m_s = \pm 1$ states are separated from $m_s = 0$ by an energy of 2.87 GHz due to spin-spin interactions. The excited orbital states lie 1.945 eV (637 nm) above the ground state and can be populated by optical transitions from the ground state spin manifold. The optical transitions are highly spin-preserving but the excited $m_s = \pm 1$ state can also decay non-radiatively into a metastable singlet state. The singlet has a much longer lifetime of 150 - 450 ns [22] and relaxes into the $m_s = 0$ ground state [4]. This enables an initialization in the $m_s = 0$ state by optical pumping. Additionally, the spin state can be read out optically because less fluorescence is detected when the spin is initially in the $m_s = \pm 1$ state and passes through the long-living singlet state [2].

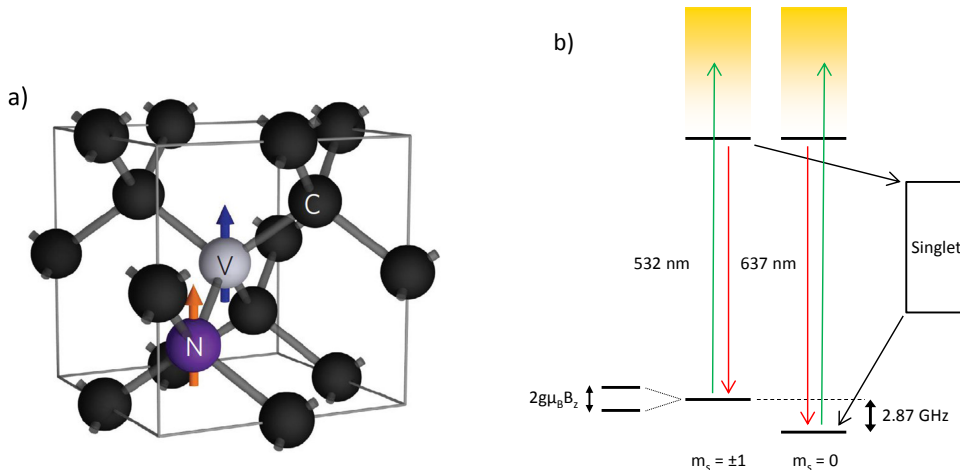


Fig. 1: **a)** Face-centered cubic (fcc) lattice of diamond including an NV center. **b)** Simplified electronic structure of the NV center with non-resonant green excitation into the phonon sideband and Zeeman splitting $2g\mu_B B_z$ of the $m_s = \pm 1$ states.

¹There is also a neutral NV^0 center which is not subject to our study and we refer to the NV^- simply as NV center.

Fig. 2 a) shows the fluorescence spectrum of the NV center at room temperature. The zero-phonon line, being the purely electronic transition, is found at 637 nm but it contains only about 4% of the fluorescence at room temperature [23]. The emission into the "phonon-sideband", involving simultaneous emission of a photon and one or more phonons, is much more dominant due to a strong electron-phonon coupling [24]. The lifetime of the excited state is about 12.5 ns for NV centers in bulk diamond (Fig. 2 b). Hence, roughly 80 million photons are expected to be emitted per second by a single NV center at saturation, considering a quantum efficiency of 100%.² Since typical experiments yield saturation count rates in the order of 100 kcps, the collection and detection efficiency is only in the order of 0.1%. To assess the angular distribution of the fluorescence, it is important to know that the emission of the NV center can be described using two electric dipoles perpendicular to each other and to the NV center symmetry axis [26]. Therefore, the emission power density in direction of the NV axis is twice as high as perpendicular to it.

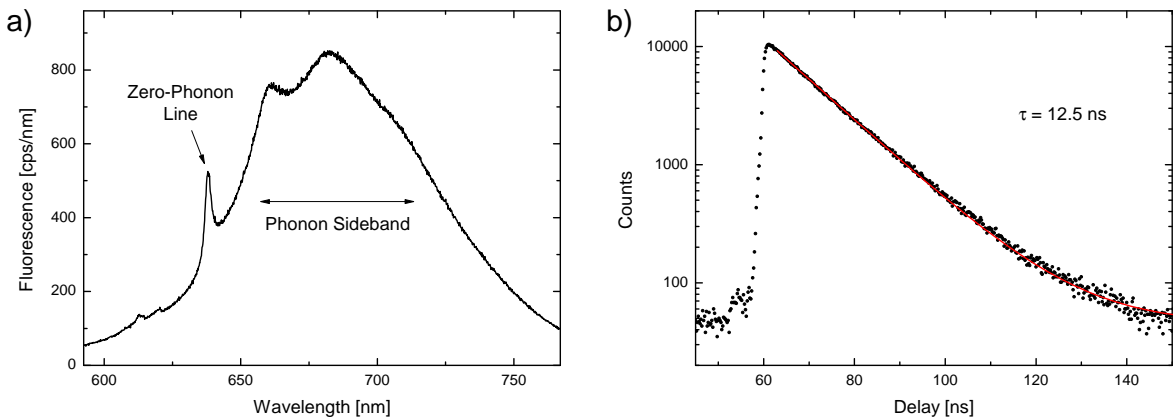


Fig. 2: a) NV center fluorescence spectrum at room temperature with non-resonant excitation at 532 nm. b) Lifetime measurement of an NV center using a pulsed laser. The red curve is a single exponential decay fit including a constant background contribution which reveals a lifetime of $\tau = 12.5$ ns.

The electron spin of the NV center can be manipulated using a microwave (MW) field. Fig. 3 a) shows the decrease in fluorescence when the MW frequency matches the transition energy from $m_s = 0$ to $m_s = \pm 1$ (electron spin resonance, ESR), where the $m_s = \pm 1$ states are split due to a static magnetic field (Zeeman effect). Rabi oscillation between $m_s = 0$ and $m_s = \pm 1$ can be performed if the MW frequency is in resonance with one of the transitions and the length of the MW pulse is varied (Fig. 3 b).

²The quantum efficiency has never been measured in bulk diamond and lower quantum efficiencies between 26% and 90% have been suggested for nanodiamonds [25].

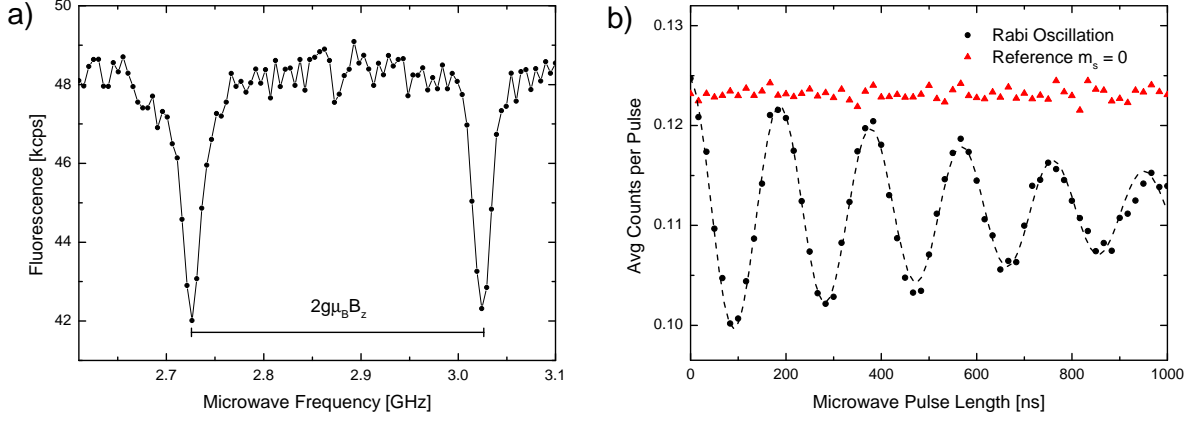


Fig. 3: a) ESR measurement with Zeeman splitting of $m_s = \pm 1$. $B_z \approx 50$ Gauss here due to a shift of 2.8 MHz/Gauss. The continuous line is only a guide to the eye. b) Rabi oscillation of a single NV center. The dashed line represents a fit with $\exp(-\frac{t}{T_d}) \cos(\Omega_r t)$, where the decay time $T_d = 780$ ns and the Rabi frequency $\Omega_r = 33$ MHz.

Finally, the coherence time T_2 can be measured by the spin echo, where the spin precesses freely for a time 2τ (Fig. 4) [27]. Several echo collapses and revivals occur due to interaction with ^{13}C nuclear spins [4].

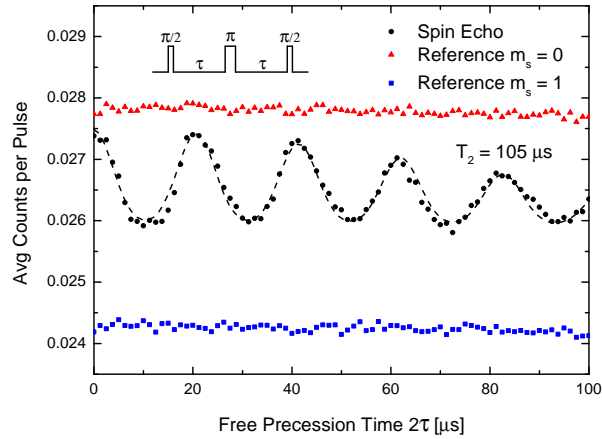


Fig. 4: Spin echo measurement of an NV center, where the coherence is preserved over several tens of microseconds. A fitting function as in [6] with an envelope $\propto \exp(-(t/T_2)^n)$ is represented by the dashed line, yielding a coherence time $T_2 = 105 \mu\text{s}$ and $n = 2.0$.

2.2 Solid Immersion Lens

Since the NV center is located in a high-refractive-index material ($n = 2.4$), the collection efficiency is usually very small because of refraction and total internal reflection at the surface. This challenge can be overcome by using a solid immersion lens (SIL) consisting of a hemisphere with refractive index n_{SIL} which is placed on the diamond surface (see Fig. 5). The effect of the SIL is to alter the refraction at the surface and to increase the collected angle in diamond and therefore the collection efficiency (see Fig. 6). The advantage of solids, as opposed to immersion oils which are often used for the same purpose, is the much higher possible refractive index of up to 3.5 for some semiconductors compared to 1.7 for the highest immersion oils. Apart from collection efficiency, the SIL also increases the resolution and the signal-to-background ratio as we will discuss in the following.

Resolution

The lateral resolution limit (FWHM) in a far-field microscope is given by

$$\Delta x \approx \frac{0.51\lambda}{\text{NA}} \quad [28]; \quad (1)$$

where λ is the vacuum wavelength and $\text{NA} = n_{os} \sin(\theta_{os})$, n_{os} being the refractive index and θ_{os} the collected half-angle in the object space [29]. The hemispherical SIL increases the NA and therefore improves the lateral resolution by a factor of n_{SIL} [30].³ This is done through increase of θ_{os} according to Snell's law

$$\frac{\sin(\theta_1)}{\sin(\theta_2)} = \frac{n_2}{n_1} \quad \text{or specifically} \quad \frac{\sin(\theta_{os})}{\text{NA}_{obj}} = \frac{n_{SIL}}{n_{diamond}} \quad (2)$$

where $\text{NA}_{obj} = \sin(\theta_{obj})$ is the objective NA and θ_{obj} the collection half-angle of the objective.

The longitudinal resolution limit is given by

$$\Delta z \approx \frac{0.44\lambda}{n_{os} \sin^2\left(\frac{\theta_{os}}{2}\right)} \quad [32] \quad (3)$$

Longitudinally, the resolution improvement using a SIL is even more significant and scales with n_{SIL}^2 for small angles θ_{os} . The improved longitudinal resolution is valuable due to a

³There is also a super-hemispherical SIL, known as Weierstrass optic [31], which offers a greater increase of the NA but suffers from chromatic aberration and is not studied here.

reduced detection volume and thus a smaller background signal. Furthermore, the "optical lever" effect in the SIL leads to a magnification by a factor of n_{SIL} in all three dimensions (Fig. 5) [29].

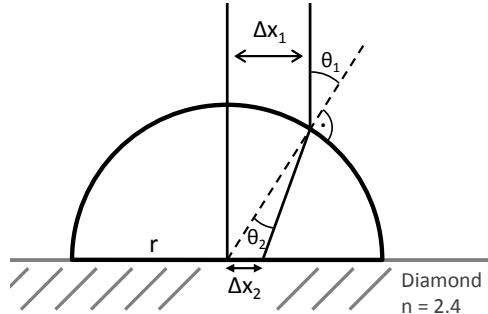


Fig. 5: Schematic explanation of the lateral SIL magnification effect. A shift of a vertically incoming ray Δx_1 results in an angle to the SIL surface θ_1 as $\frac{\Delta x_1}{r} = \sin(\theta_1)$. Further, $\frac{\Delta x_2}{r} \approx \sin(\theta_2)$ for small shifts $\Delta x_1 \ll r$. Therefore the magnification is given by $\frac{\Delta x_1}{\Delta x_2} \approx \frac{\sin(\theta_1)}{\sin(\theta_2)} = n_{SIL}$.

Collection Efficiency

In this work, the increased collection efficiency using a SIL is of major interest. The collection efficiency for an isotropic emitter is given by the ratio of the collected solid angle in the object space to the total solid angle 4π . For a certain angular semi-aperture θ_{os} , the collected solid angle is given by

$$\int_0^{2\pi} d\phi \int_0^{\theta_{os}} \sin(\theta) d\theta = 2\pi(1 - \cos(\theta_{os})) \quad (4)$$

where θ is again the angle to the optical axis ϕ the angle around that axis. Therefore the collection efficiency η amounts to

$$\eta(\theta_{os}) = \frac{1}{2} - \frac{1}{2} \cos(\theta_{os}) \quad [29] \quad (5)$$

Using a SIL increases the NA by a factor of n_{SIL} which leads to a significant enhancement of collection efficiencies by a factor of at least n_{SIL}^2 (small angle approximation). Furthermore, since the excitation and collection volume decreases with $\sim 1/n_{SIL}^4$ (resolution improvement in all dimensions), the signal-to-background ratio is expected to scale with $\sim n_{SIL}^4$, assuming a homogeneous background. Fig. 6 explains schematically how the collection angle is increased using a SIL and the calculated collection efficiencies are provided in table 1.

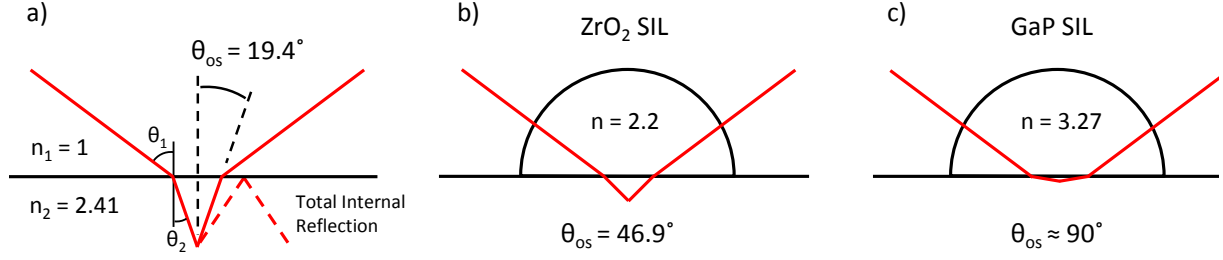


Fig. 6: The collected half-angle θ_{os} of an emitter in diamond increases dramatically using a high-index SIL. Note that with the GaP SIL, the theoretical θ_{os} can only be realized very close to the surface, since a strong aberration occurs at the diamond-GaP interface due to the large index contrast. The values are calculated for $NA_{obj} = 0.8$.

	no SIL	ZrO ₂ SIL	GaP SIL
n_{SIL} at 680 nm	1	2.20	3.27
NA	0.8	1.76	2.41
θ_{os}	19.4°	46.9°	90° ⁴
η	2.84% (2.19% - 4.13%)	15.8% (13.6% - 20.4%)	50%
η incl. reflections ⁵	2.35% (1.81% - 3.43%)	13.6% (11.6% - 17.5%)	35.0% ⁶
efficiency gain	-	5.8 (5.1 - 6.4)	15 (10 - 19) ⁶

Table 1: Calculated for an objective NA = 0.8 and $n_{os} = 2.41$ (diamond). The values before the brackets are for isotropic emission and those in brackets consider the NV center emission in two dipoles. The lowest efficiencies represent the orientation with one perpendicular dipole and for the highest efficiencies both dipoles are oriented parallel to the surface (see Appendix for more details).

⁴NA and θ_{os} limited by collection of the entire half space.

⁵Reflections at the interfaces diamond-air or diamond-SIL and SIL-air as $R = \left(\frac{n_1 - n_2}{n_1 + n_2}\right)^2$

⁶The higher excitation wavelength of 560 nm needed for transmission through the GaP SIL leads to a lower NV center fluorescence of about 80% compared to 532 nm excitation [33]. Roughly 10% are absorbed in 1 mm GaP [34]. Therefore, the collection efficiency is rather around 25%.

2.3 Dielectric Antenna

The dielectric antenna is a design which allows an even higher collection efficiency than using a SIL. It has long been discovered that when an emitter is located in the vicinity of an interface with a higher refractive index medium, some of the light is emitted beyond the critical angle in the denser medium by evanescent coupling [35]. Lukosz and Kunz calculated the angular power density of the emitted light for different distances z_0 to the interface, where generally more light is emitted into the denser medium (Fig. 7) [36].

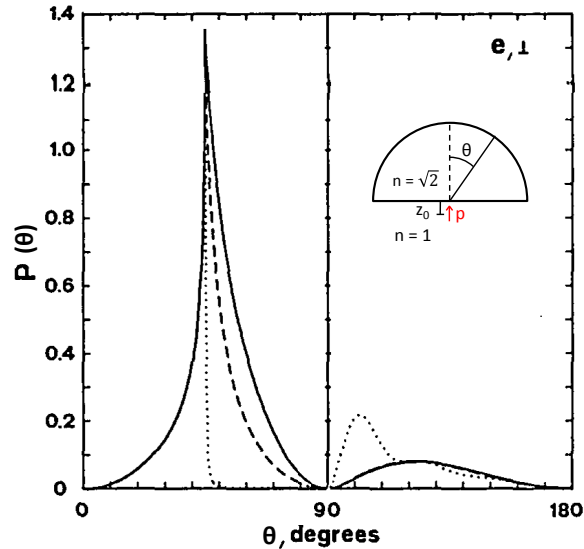


Fig. 7: Normalized angular power density of light emission $P(\theta)d\Omega$ for an electric dipole perpendicular to the interface. $z_0 = 0$ (continuous line), $z_0 = \lambda/4\pi$ (dashed line) and $z_0 = \lambda$ (dotted line). The closer the emitter to the denser medium, the more light is emitted into the denser medium beyond the critical angle. The relative refractive index $n_2/n_1 = \sqrt{2}$ and the critical angle lies at 45° . Graph taken from [36].

In a dielectric antenna however, three materials $n_1 < n_2 < n_3$ with two interfaces are used. The emitter is located roughly in the center of the thin middle layer of index n_2 and most fluorescence is guided into the denser medium (Fig. 8 a). In contrast to an emitter close to a single interface as described above, this happens at larger distances to the interfaces $z_0 \geq \frac{\lambda}{n}$ and therefore with only little evanescent coupling and little emission beyond the critical angle in the denser medium. The angular radiation pattern of such a structure was first measured and simulated by Luan et al. [18]. Lee et al. reported a 96% collection efficiency using molecules with perpendicular dipoles in a thin polymer layer on a sapphire SIL [20]. The simulations in Fig. 8 b) for a dielectric antenna with diamond and GaP show that the emission peaks at the critical angle and virtually no light occurs at larger angles. This is important for high collection efficiencies at a realistic NA_{obj} . For parallel dipoles, more light is collected at smaller angles, but in the same dielectric

antenna geometry the collection efficiency is lower due to higher losses into the thinner medium. These losses could only be avoided with an additional mirror in the thinner medium [19]. The thickness of the middle layer can be between $0.5 \mu\text{m}$ and several μm , such that the layer represents a quasi-waveguide, meaning it would be a good waveguide in absence of the higher index material [20].

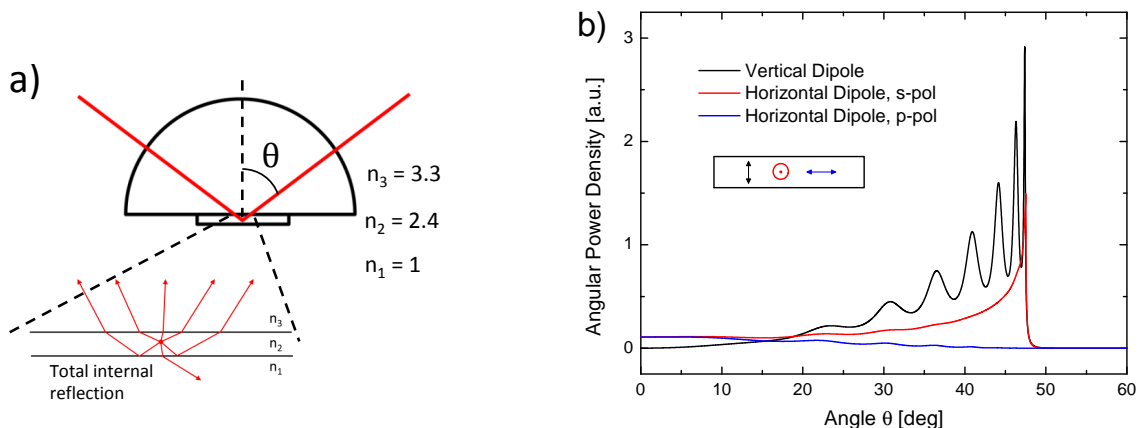


Fig. 8: **a)** Schematic representation of a dielectric antenna with a thin diamond piece and a GaP SIL, including a simplified geometric explanation of the directional emission. **b)** Simulations for the angular emission distribution in a dielectric antenna with a $1 \mu\text{m}$ thick diamond piece and GaP. Three different orientations of the dipole located in the center of the diamond layer are simulated for an emission wavelength of 680 nm . Emission maxima occur at the critical angle of diamond-GaP. Calculation according to [18] presented in the Appendix.

2.4 Back Focal Plane Imaging

Back focal plane imaging is a method to measure the angular distribution of the collected light [20] which can be used to determine the orientation of a dipole emitter [37]. As described by Fourier optics, the back focal plane of a lens (or objective) represents the Fourier transform of the object in the focal plane [38]. Each point in the back focal plane image (k_x, k_y) can be assigned to an emission angle (θ, ϕ) by

$$\frac{k_{\perp}}{|\vec{k}|} = \frac{\sqrt{k_x^2 + k_y^2}}{|\vec{k}|} = \sin(\theta) \quad \text{and} \quad \frac{k_y}{k_x} = \tan(\phi) \quad (6)$$

θ being the angle to the optical axis and ϕ the angle around that axis. When ideally only one emitter is excited, the back focal plane image reveals its angular emission characteristics allowing to reconstruct the dipole orientation (Fig. 9).

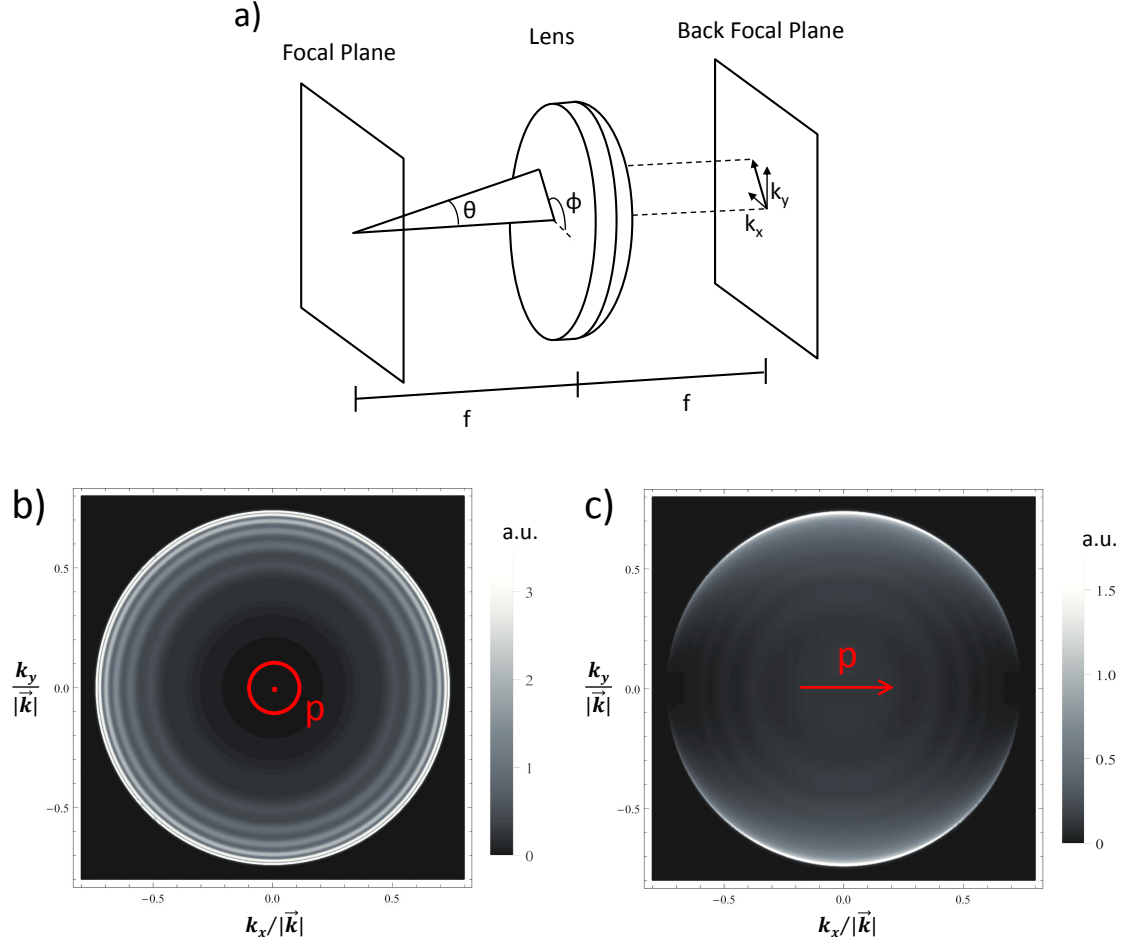


Fig. 9: a) Illustration of the correlation between emission angle and back focal plane image. b) and c) Simulated back focal plane images for the diamond-GaP dielectric antenna as in Fig. 8 b).

The recorded back focal plane image $P(k_x, k_y)$ is converted to the angular power density $P(\theta)$ as follows:

$$\begin{aligned}
 P(k_x, k_y) dk_x dk_y &\rightarrow P(k_\perp, \phi) k_\perp dk_\perp d\phi = P(k_\perp, \phi) \sin(\theta) d \sin(\theta) d\phi = \\
 &= P(k_\perp, \phi) \cos(\theta) \sin(\theta) d\theta d\phi = P(k_\perp, \phi) \cos(\theta) d\Omega
 \end{aligned} \tag{7}$$

and therefore

$$P(\theta) d\Omega = P(\arcsin(k_\perp/|\vec{k}|)) \cos(\theta) d\Omega \tag{8}$$

where Ω is the solid angle. Practically, to obtain $P(\theta) d\Omega$, the back focal plane $P(k_x, k_y)$ is first used to calculate the average cross-section $P(k_\perp)$. It is then converted to $P(\theta)$ using the arcsine and normalizing the edge of the back focal plane image to NA_{obj} . Finally, it is corrected by the factor $\cos(\theta)$.

3 Materials and Methods

3.1 Confocal Microscope

The core of the experimental setup employed in this work consists of a confocal microscope with a green excitation path and a red collection path. For excitation, either a 532 nm CW diode laser or a pulsed supercontinuum laser (SuperK Extreme EXW-12) was used. The latter is combined with a tunable bandpass filter with variable bandwidth (2 - 10 nm) and center wavelength (530 - 600 nm) to excite NV centers through the GaP SILs and operated at a pulse rate of 78 MHz. The setup is confocal because of the overlaying diffraction limited excitation and detection spot using single-mode fibers and therefore yields a small detection volume and background signal.

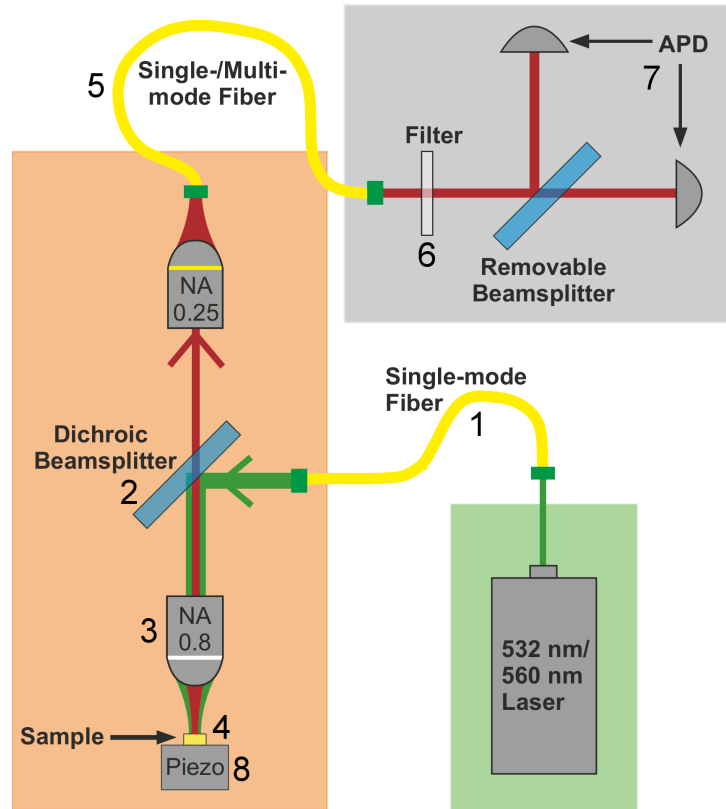


Fig. 10: Setup of the confocal Microscope. After a single-mode fiber (1), the excitation beam is collimated by a lens and then reflected by a dichroic beamsplitter (2) and focused on the sample (4) by a 0.8 NA objective (3). The fluorescent light is then collected and collimated by the same objective, passes through the dichroic beamsplitter and is coupled into another single-mode fiber (5) (unless stated otherwise). To avoid scattered laser light and shorter wavelength non-NV fluorescence, the light passes a 600 nm longpass filter (6) and is then focused on one or two avalanche photodiodes (APDs, 7). The sample is positioned on a piezoelectric actuator (Attocube, 8) by which the sample can be scanned in all three dimensions to create images.

3.2 Back Focal Plane Imaging Setup

To resolve the angular distribution of the collected fluorescence, the back focal plane of the objective was imaged with a CCD camera (Watec WAT-910HX, see Fig. 11). Instead of coupling the fluorescence into the fiber, the light is deflected from the optical axis of the microscope detection arm and sent towards the back focal plane imaging arrangement. It is focused, passes a 500 μm pinhole for background reduction, is collimated and focused again. The back focal plane is imaged (black dotted lines) when the CCD is placed about 2 cm behind the focal plane image at the second crossing of the parallel beams (red lines).

The inset image in Fig. 11 shows a recorded back focal plane image where the sharp bright circle in the center represents the back focal plane of the collected fluorescence. The illuminated back side of the objective, which is imaged simultaneously, is not perfectly focused, indicating that it is slightly shifted with respect to the back focal plane. To additionally verify correct alignment of our back focal plane imaging setup, we coupled a collimated laser beam into the front lens of the microscope objective. This collimated beam was mapped to a focussed spot in the back focal plane as expected. Regular images of the samples (focal plane) could be recorded by moving the CCD by 2 cm.

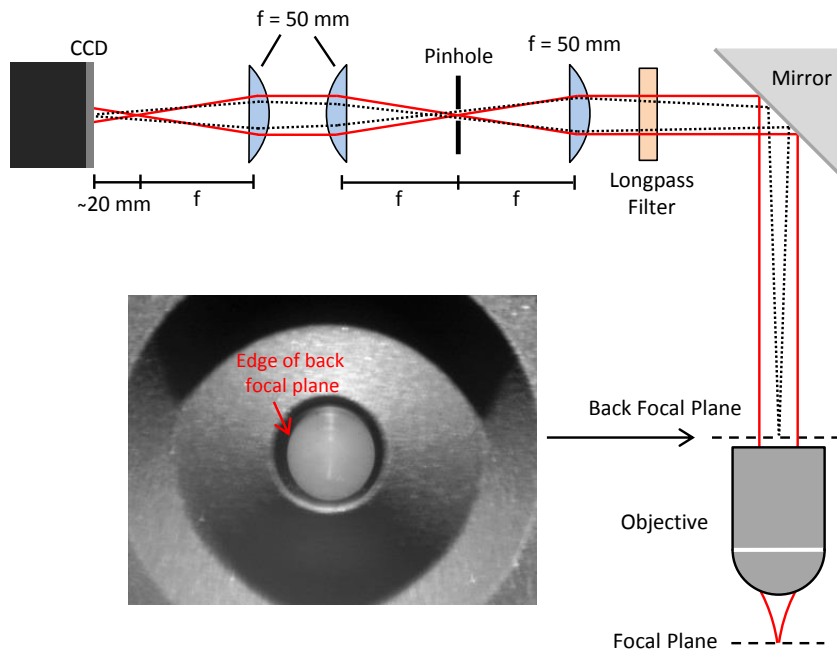


Fig. 11: The setup to image the back focal plane, where the red lines represent rays from the sample in the focal plane and the black dotted lines illustrate the focussing of the back focal plane on the CCD. The inset shows an example image with an illuminated back side of the objective. The back focal plane shows a practically isotropic emission from a CVD diamond and a very bright emission from tens of NV centers with an equivalent of several million counts on the APD.

3.3 SILs

Commercially available ZrO_2 and GaP hemispherical SILs with a diameter of 2 mm were used. The SILs originally had a poor surface quality which had to be improved to assure proper adhesion of the SIL to the sample surface. However, a few minutes of polishing with a grain size of $0.25\ \mu\text{m}$ were sufficient to eliminate the scratches on the planar side of the SILs (Fig. 12). Polishing was also used to increase the planarity of the GaP SILs, though with limited success. Both before and after polishing, the unevenness was visible to the naked eye through the distortion of the reflection at the flat side of the GaP SILs. No planarity issues were observed with the ZrO_2 SILs.

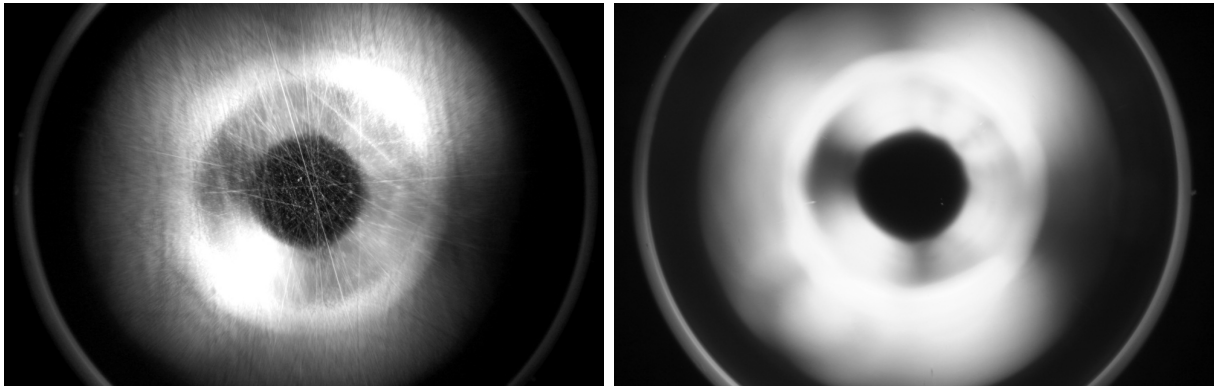


Fig. 12: Dark-field image of a ZrO_2 SIL before and after polishing. Both focused on the flat side through the SIL.

Since the contact quality between the sample and the SIL is critical for the collection efficiency, different mounting techniques of the SIL to the diamond surface were evaluated. The first approach consisted in using evaporation of distilled water between the SIL and the sample as an adhesion promoter. Good adhesion of the SIL to the sample was achieved, albeit with large fluctuations in quality and gap size. Another possibility is to use vacuum grease (Dow Corning) to mount the SIL. Here, it is important that not too much grease is used to minimize the gap between sample and SIL. It was found that for very clean and planar samples and SILs a robust contact and the highest collection efficiencies were obtained just by pressing the SIL on the sample without the use of grease or water. For uneven surfaces, the use of little vacuum grease enhances the stability of the contact and possibly enhances the collection efficiency in presence of a gap through increasing the refractive index in the gap from 1 to 1.3. Compared to the use of water evaporation, the use of no or little grease and pressing the sample on was found to be a more reliable technique, and it was possible to estimate the gap size from the interference colors below the SIL (see Fig. 24 a). The presence of interference colors meant a large gap while no colors typically meant a very small gap (good contact).

For the dielectric antenna experiment, thin diamond slabs or cantilevers were broken off above the inverted SIL and positioned in the center of the SIL using a Narishige micromanipulator (Fig. 13).

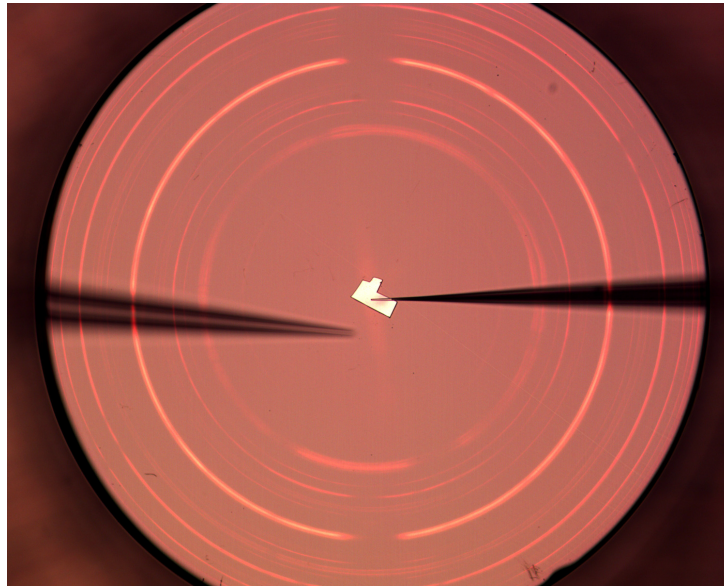


Fig. 13: Using glass needles in a micromanipulator to position a diamond slab on a GaP SIL.

4 Results and Discussion

4.1 ZrO₂ SIL

4.1.1 Resolution Measurement

As a first experiment, the resolution enhancement by the ZrO₂ SIL was tested with a 4 μm period line grating of chromium on glass (Fig. 14 a). The reflection of the sample was measured as a function of the position. The resolution is determined by the width of the transition from the dark to the bright area. Fig. 14 b) shows a well contacted SIL, which was mounted with a very small amount of vacuum grease and properly pressed on (see Sect. 3.3) where a sharp contrast between the bright and dark regions is recognizable. A badly contacted SIL can be seen in Fig. 14 c) where the SIL surface (bright horizontal line) and the line grating (bright squares) are separated by about 2 μm . In this case, the SIL was mounted with water evaporation which resulted in large fluctuations of the contact quality. Apparently, the resolution and the contrast is reduced when an air gap is present between sample and SIL.

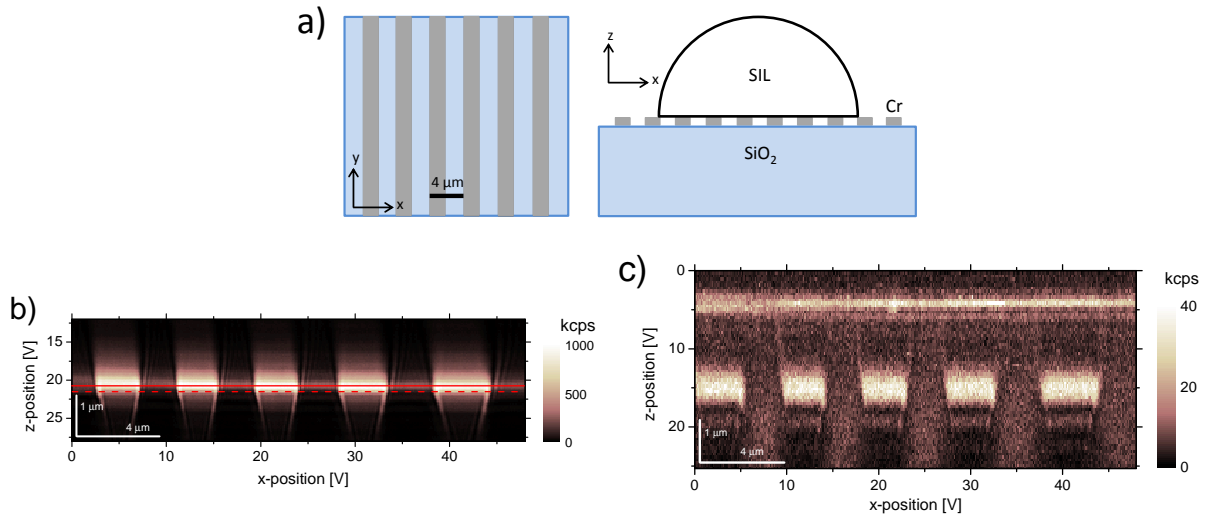


Fig. 14: **a)** Schematic orientation over the line grating. **b)** and **c)** Reflected intensity as a function of the z - and x -position using a ZrO₂ SIL. The SIL is located in top of the image and the bright areas represent cuts through the chrome lines. 532 nm laser light and a 532 nm band pass filter before the APD are used to avoid fluorescent light. In **b)**, a good contact between SIL and line grating is present and a relatively weak reflectance is seen from the ZrO₂-glass interface between the Cr lines. The red lines indicate the height at which a detailed line scan is made (fig. 15). In **c)**, a large gap between SIL and sample is observed. The distance indicators are approximations and subject to piezo nonlinearity.

Fig. 15 a) shows a line scan along the continuous red line in Fig. 14 b). The spatial resolution is determined to be 140 ± 17 nm (FWHM in the derivative), which lies between

the predicted confocal diffraction limit of 111 nm and the non-confocal limit of 153 nm for our setup. Note that a slightly different z-position yields a different calculated resolution of 110 ± 10 nm due to "overshoots" (Fig. 15 b). We assign these overshoots to interference effects and therefore discard these values. Without the SIL, we determined a spatial resolution of 300 ± 50 nm (data not shown), in accordance with the theoretical confocal value of 246 nm. The resolution enhancement using a ZrO_2 SIL was therefore successfully demonstrated in our experiment.

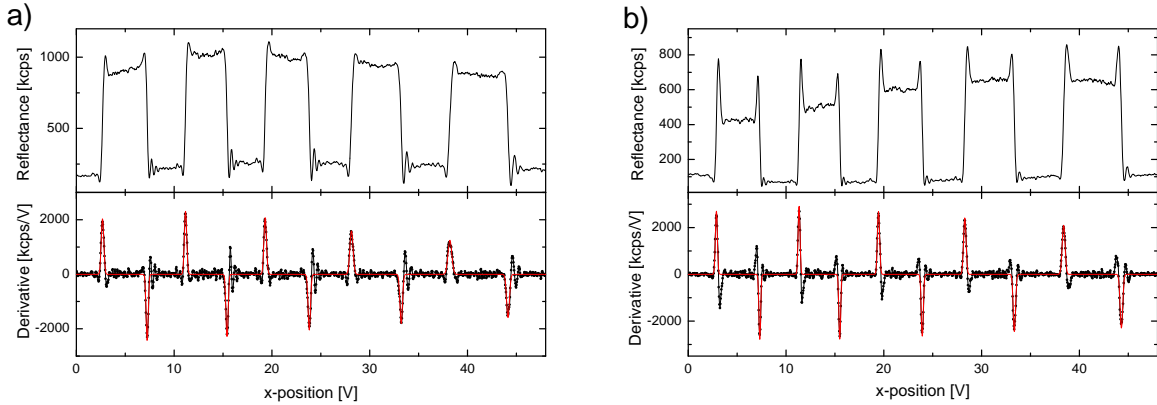


Fig. 15: **a)** Line scan through the 4 μm period grating along the continuous red line Fig. 14 b). A resolution of 140 ± 17 nm is determined by the FWHM of Gaussians fits to the derivative. **b)** Large overshoots are observed at a slightly different z-position (dashed red line). This leads to a better calculated resolution of 110 ± 10 nm, which has to be approached with caution. The drifts in brightness across the x-positions probably originates in a small tilt of the sample.

4.1.2 ZrO_2 SIL on Bulk Diamond

As an application of our ZrO_2 SIL, we performed confocal imaging of NV centers in a polycrystalline CVD diamond sample with and without SIL and compare the two cases. Fig. 16 a) shows a confocal scan without SIL, where many singly resolved NV centers are observed. The background signal is relatively high due to a large detection volume, especially where a high NV concentration is present. Only a few isolated NV centers with low background signal and representative count rates are found (red circle).

The same area is found again under a ZrO_2 SIL, where the increased resolution is easily recognized in the smaller spot sizes (Fig. 16 b). The much brighter NV centers demonstrate the improved collection efficiency with the SIL, where at the same time the background is smaller due to the decreased depth of field. This superior signal-to-background ratio is also seen in the smaller $g^2(0)$ values which are around 0.1 using the SIL (Fig. 16 c). The presence of a very good contact between sample and SIL is shown in Fig. 16 d).

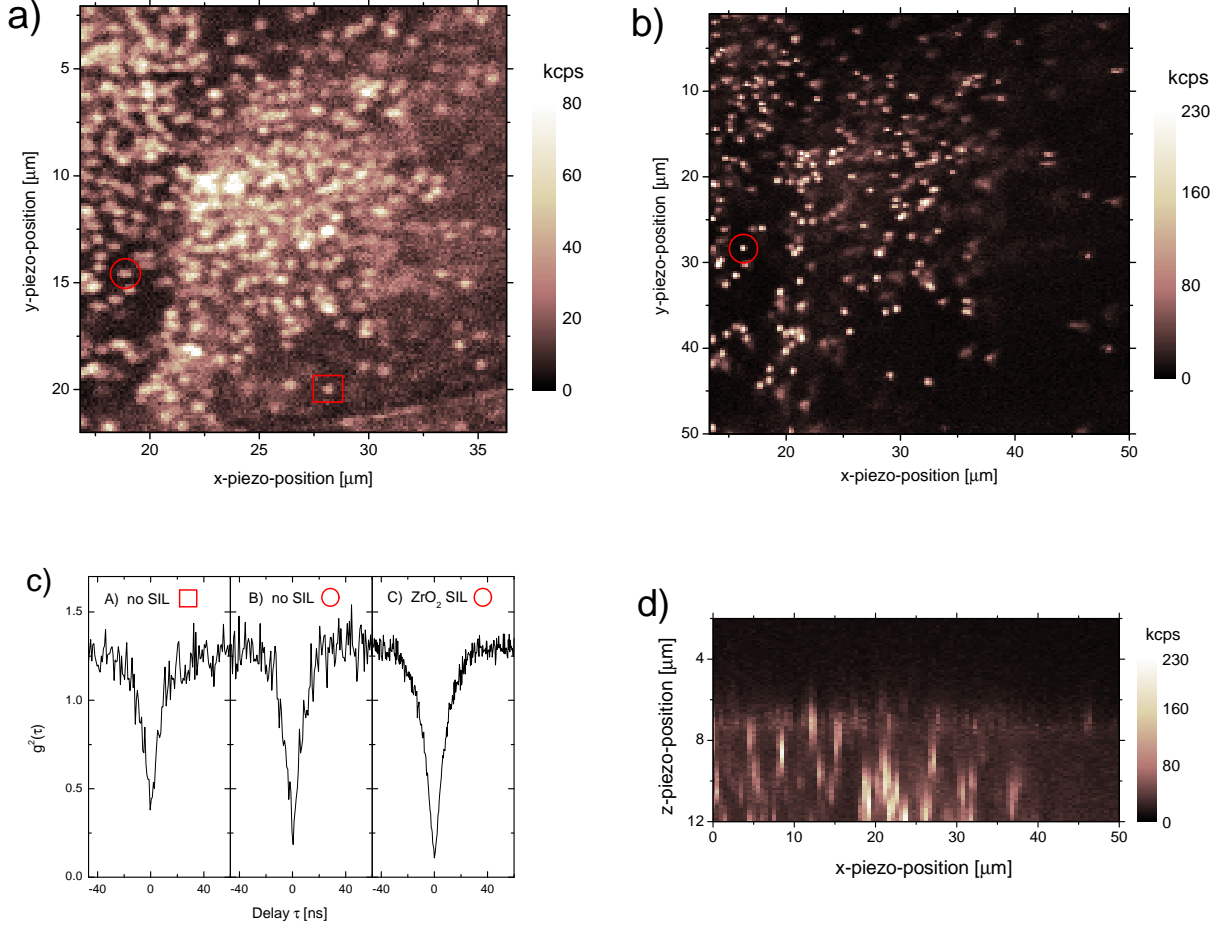


Fig. 16: **a)** Fluorescence distribution in a polycrystalline diamond without SIL at excitation intensity close to saturation ($800 \mu\text{W}$), where the bright spots are NV centers. The well isolated NV center in the red circle was further examined regarding $g^2(\tau)$ and saturation curve (Fig. 16 c) and 17 a). **b)** Same field of view as a) using a ZrO_2 SIL also at $800 \mu\text{W}$. The SIL was mounted without vacuum grease or water evaporation. Some NV centers are not visible here due to the smaller depth of field. Better resolution, higher collection efficiency and a magnification are apparent. **c)** Second-order correlation function $g^2(\tau)$ at $400 \mu\text{W}$ (A) and B) and $80 \mu\text{W}$ (C), normalised to $\tau \rightarrow \infty$. A) and B) are two single NV centers from a) in the red square and circle, respectively. The latter has a lower $g^2(0)$ value of 0.2 compared to 0.4, which confirms a smaller background signal already observed in the scan. C) shows the same NV center in the red circle but with use of a ZrO_2 SIL (b). Here, the superior signal-to-background ratio leads to a lower $g^2(0)$ value of 0.1, which is supposedly strongly limited by the electronic response time of the detection setup. The measured background of 0.5% of the NV center count rate would suggest a $g^2(0) \approx 0.01$. **d)** z-x-scan showing the boundary between the diamond and the ZrO_2 SIL in the same area as before at $800 \mu\text{W}$. The 600 nm longpass filter before the APD was removed to allow for reflected laser light. The near absence of a signal at the diamond-SIL interface indicates a very good contact, which was facilitated by the use of a $200 \mu\text{m}$ diameter diamond mesa.

To compare the collection efficiency with and without SIL, the saturation curve of the same NV center (red circle) is recorded in both cases and fitted to the saturation function

$$I(P) = \frac{I_0}{1 + \frac{P_0}{P}} + aP \quad (9)$$

where I is the count rate, I_0 the saturation count rate, P the excitation power, P_0 the saturation power and a the linear background contribution (Fig. 17 a). We find a saturation count rate of 75 ± 2 kcps without and 325 ± 3 kcps with ZrO_2 SIL, which indicates a factor of 4.3 improvement in collection efficiency using the SIL. This is still somewhat lower than the theoretical factor of 5.8, which we assign to losses due to a still imperfect diamond-SIL contact or a non-zero roughness of the spherical surface of the SIL. Additionally, the saturation power with SIL is about 4 times lower which is due to the smaller focus size (higher resolution) resulting in a higher excitation intensity at same laser power. For consistency, we measured the collection efficiency improvement also in an electronic grade diamond, where we determined again an enhancement by a factor of roughly 4 (Fig. 17 b). However, for an unknown reason, NV centers in the electronic grade diamond yielded somewhat lower saturation count rates and higher saturation powers.

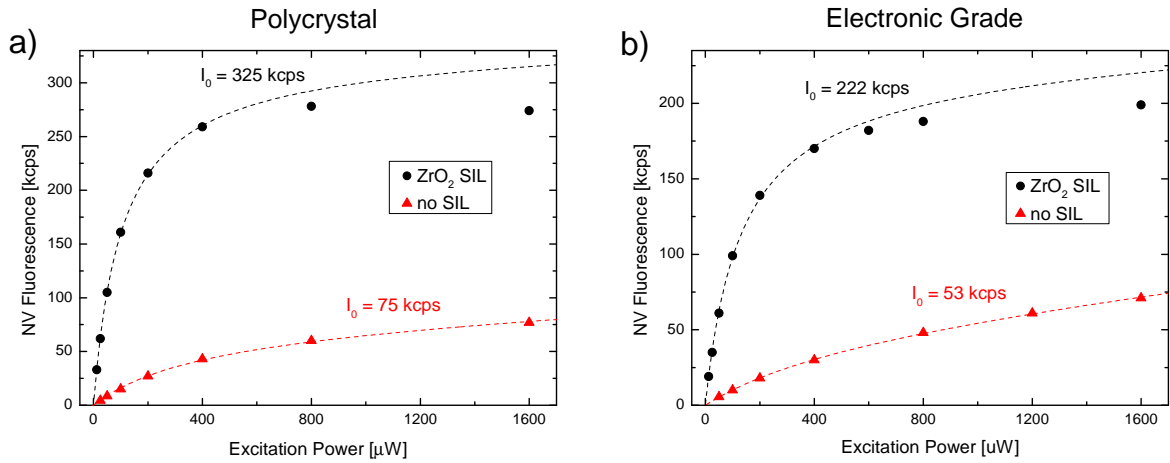


Fig. 17: a) Measured count rate of the NV center indicated with the red circle in Fig. 16 a) and b) for different excitation powers with and without ZrO_2 SIL. **Without SIL**, the fit yields $I_0 = 75 \pm 2$ kcps, $P_0 = 397 \pm 24$ μW and $a = 11.3$ cps/ μW . **With SIL**: $I_0 = 325 \pm 3$ kcps, $P_0 = 104 \pm 2$ μW and $a = 6.2$ cps/ μW . The last two data points are excluded from the fit with SIL because the count rate is lowered assumingly by blinking (changing to charge state NV^0 at high powers) which was realized in a poor fit quality using all points. b) Count rates in electronic grade diamond with and without ZrO_2 SIL. **Without SIL**: $I_0 = 222 \pm 4$ kcps, $P_0 = 129 \pm 6$ μW and $a = 9.4$ cps/ μW . **With SIL**: $I_0 = 53 \pm 1$ kcps, $P_0 = 557 \pm 26$ μW and $a = 20$ cps/ μW . The points above 400 μW with SIL are again excluded from the fit.

4.2 GaP SIL

Encouraged by our results with the ZrO₂ SIL, attempts were made to reproduce these experiments using GaP SILs. This material is highly attractive for photonics applications due to its record-high refractive index of $n = 3.3$, which would further improve the fluorescence collection efficiency over the ZrO₂ SIL. However, several additional challenges had to be addressed with the GaP SILs and will be discussed in this section. One was that 532 nm excitation light is fully absorbed in GaP due to its band gap of 2.26 eV (549 nm). In order to determine the optimal excitation wavelength, we measured the transmission spectrum through the SIL using a white light source and a spectrometer (fig. 18). GaP becomes transparent at 555 nm the transmission further improves with higher wavelengths. Due to the photo-physics of the NV center [33], we want a wavelength as close to 532 nm as possible. Therefore, for the use of the GaP SILs an excitation wavelength of 560 nm forms a good compromise between GaP transmittance and optimal NV fluorescence excitation.

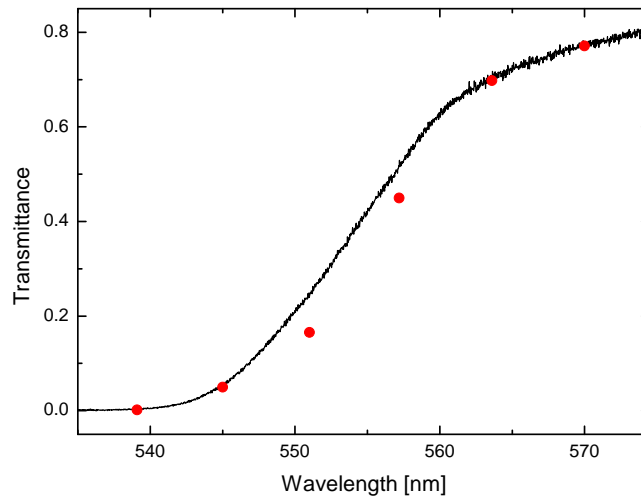


Fig. 18: Normalized transmission through a GaP SIL of 1 mm radius, not considering the reflection at both surfaces. The literature values (red points) are calculated from the tabulated absorption coefficients in [34] and the measured curve is normalized to the literature value at 570 nm. According to [34], the absorption in the main NV fluorescence range of 630 - 730 nm for 1 mm GaP is still around 10% due to impurities.

4.2.1 Resolution Measurement

To assess the performance of the GaP SIL, we repeated the experiments described in Sect. 4.1.1. When the SIL is mounted on the line grating, no gapless contact is achieved probably because of the uneven surface of the GaP SIL (Fig. 19 a) and b). The calculated

resolution is 96 ± 5 nm which is significantly better than the resolution with the ZrO_2 SIL and again lies between the values expected from the confocal diffraction limit of 76 nm and the non-confocal limit of 104 nm (Fig. 19 c). However, since a gap is present and dominant overshoots of the reflection signal are found at the edges, this result has to be approached with caution. The spot sizes of NV centers in later scans indeed indicate a lower real resolution.

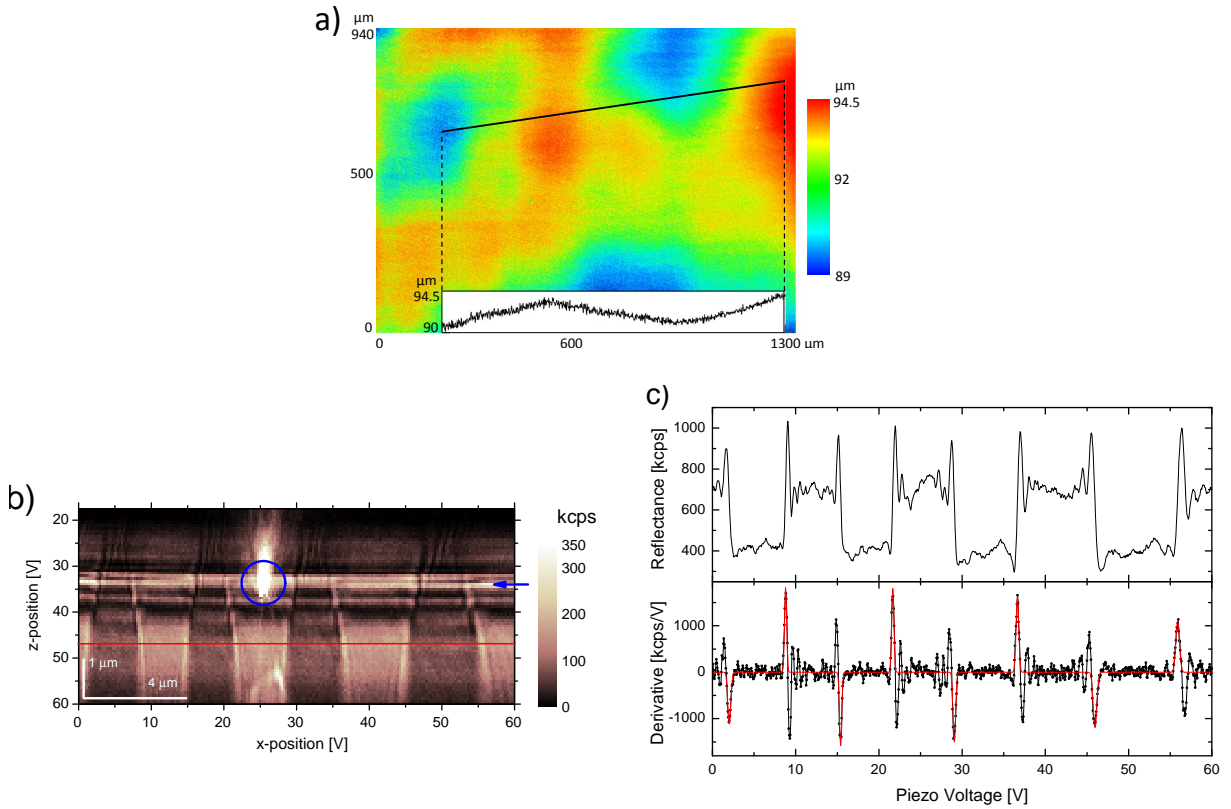


Fig. 19: **a)** 3D laser scanning microscope image (Keyence VK-X200) showing the height profile of the flat surface of the GaP SIL. Height differences of several μm confirm the relatively low planarity also observable by eye in the distorted reflection **b)** Reflected intensity in a z-x-scan through the $4 \mu\text{m}$ period chrome line grating using a GaP SIL. The surface of the SIL is indicated by the blue arrow and was identified by the continuous horizontal line of reflected light. The grating itself is mapped $1 - 2 \mu\text{m}$ below and interference patterns are observed inside the gap. The bright spot indicated by the circle marks the center of the SIL where the excitation light falls perpendicularly on the top (spherical) surface of the SIL and is reflected exactly backwards. The red line is the position the line scan presented in **c)** Line scan through the grating. The spatial resolution determined from the fit is 96 ± 5 nm. However, strong overshoots are observed at the borders, supposedly due to the bad contact quality. The reflecting and non-reflecting areas show very inconstant intensities, which additionally adds to the uncertainty in determining the spatial resolution.

4.2.2 GaP SIL on Bulk Diamond

Mounting the GaP SIL on the polycrystalline diamond, a gap between sample and SIL was not avoidable either (Fig. 20). Clearly, two reflectivity maxima in z-dimension can be observed at the two surfaces, where the upper one is much narrower indicating that the resolution (at least in z-direction) is heavily decreased after the gap. The bright spot is again caused by the light reflected at the spherical surface of the SIL.⁷

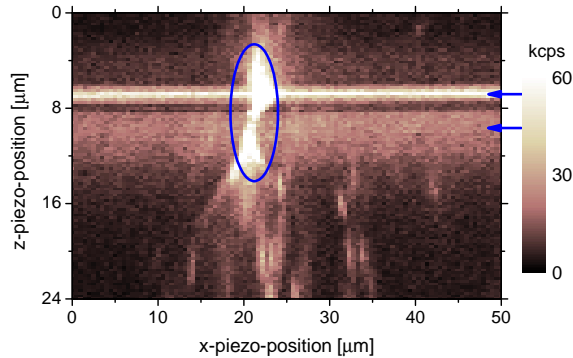


Fig. 20: z-x scan through the polycrystalline diamond and GaP SIL at 800 μW , where an apparent is observed despite careful pressing on of the SIL. This was recorded on the bulk part of the diamond (no mesa), but no better results were found on the diamond mesa. The arrows indicate the reflecting flat surfaces of diamond and SIL and the oval indicates the reflection at the spherical surface of the SIL.

Unsurprisingly due to the gap, the count rate and therefore the collection efficiency was much smaller than theoretically predicted. We experimentally determined a saturation count rate of 70 kcps for single NV centers which is comparable to the case without SIL. Additionally, with the GaP SIL the NV centers have almost the double spot size compared to ZrO_2 SIL or without SIL (spot size in terms of piezo distance). Therefore, the resolution improvement cannot compensate the magnification effect of the SIL suggesting that the resolution with GaP SIL could even be worse than with the ZrO_2 SIL.

An interesting effect observed in Fig. 21 a) is that the NV centers in the center of the image (which was also the center of the SIL) were brighter than those in the periphery for a given excitation power. By slightly misaligning the excitation beam with respect to the collection beam, the region of the brightest NV center fluorescence could be shifted from the center (Fig. 21 b): The strong dispersion in GaP leads to a different optical lever effect and therefore a different location of green excitation and the collection away from

⁷Note that the shape of this reflection spot is a convenient indicator for the sphericity of the SIL. While in the case of the ZrO_2 SIL, we found nearly diffraction limited Gaussian reflection spots the distorted shape in case of the GaP indicates a lower sphericity.

the center of the SIL (see scheme in Fig. 22). This indicates that care has to be taken in employing GaP as a SIL material and optimal signal collection efficiency can only be achieved in the very center of the SIL.

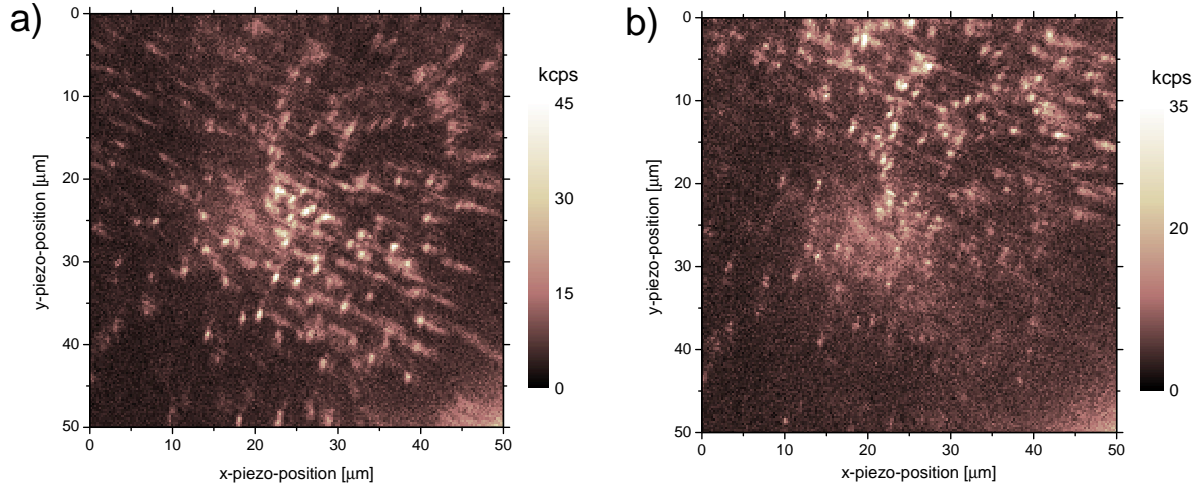


Fig. 21: a) Fluorescence inside the polycrystalline diamond using a GaP SIL at 1.2 mW excitation power. The low count rates are probably caused by the gap between sample and SIL and the NV centers in the middle are brighter due to chromatic aberration. b) Same scan as a) but with a misaligned excitation beam. The NV centers are brighter in top of the image, where the misalignment compensates for the chromatic aberration. The increased background in the center of the image comes from the light reflected at the spherical side of the SIL.

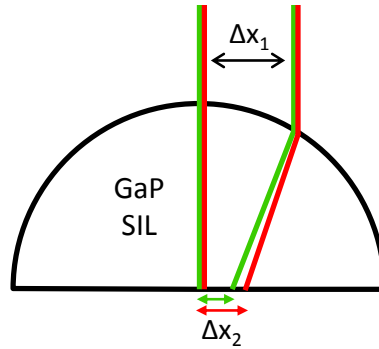


Fig. 22: Schematic explanation of the chromatic aberration in the GaP SIL. In the center of the SIL, the excitation and collection foci lie at the same position since the beams are perpendicular to the surface and are not refracted. When moving away from the center however, the green excitation beam is refracted stronger than the red one due to the higher refractive index ($n = 3.43$ at 560 nm compared to $n = 3.27$ at 680 nm, representing an approximately 10 times stronger dispersion than in ZrO_2). The chromatic aberration can also be observed in the dark-field image through the GaP SIL (Fig. 25 c)).

A further possibility for the reduced count rate with the GaP SIL is inefficient coupling into the single-mode fiber. This could be caused by aberrations due to a low sphericity of the SIL. To check this hypothesis, we used a multi-mode fiber which results in a wider collection volume and is less prone to aberrations. A saturation count rate of 140 kcps was measured and effective count rates of 80 kcps without background at a power of 900 μW . This means a factor of 2 in collection efficiency compared to the single-mode fiber, but still much less than theoretically expected. Therefore, we assume that the gap between diamond and SIL causes the most significant losses.

Another effect using the GaP SIL is seen in detail in Fig. 23, and also observable in the previous images (Fig. 21 a) and b): The slightly defocused NV centers are not imaged as round spots but as short lines pointing in two perpendicular directions depending on whether they are over- or under-focused. This means that the collection focus is strongly distorted which might either be caused by a tilted gap between SIL and sample or by a low sphericity of the SIL. This distortion has only been observed with a GaP SIL and not with ZrO_2 SILs.

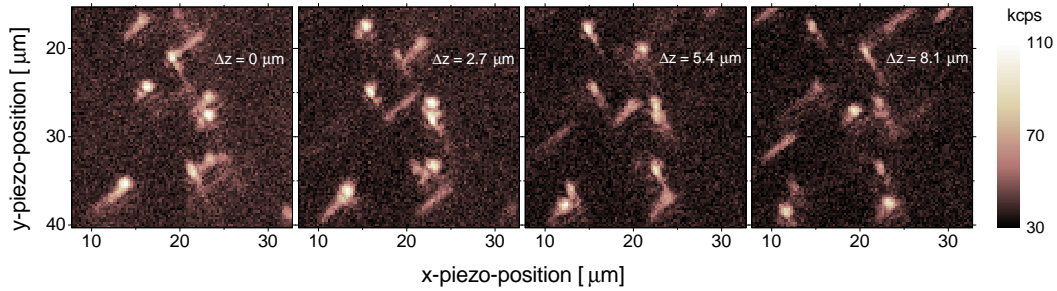


Fig. 23: Focus series in the same polycrystalline diamond, using a multi-mode collection fiber and 900 μW excitation power. Larger Δz means a focus deeper inside the diamond. Higher count rates compared to Fig. 21 are observed due to the multi-mode fiber used for this measurement. The transformation from line to circle to perpendicular line can be observed for most NV centers.

4.3 Thin Diamond Slabs and Cantilevers

In order to obtain higher collection efficiencies, thin slabs of diamond were transferred to the flat side of the SIL. On the one hand, the use of small slabs should facilitate a good contact and a smaller air gap between diamond and SIL due to a smaller contact area. On the other hand, it should be possible to create a dielectric antenna with thin diamond pieces on a GaP SIL, which yields directional emission and near-unity collection efficiency.

4.3.1 ZrO₂ SIL

As a first step, thin CVD diamond slabs with lateral dimensions in the order of 100 μm and a thickness of 1 - 5 μm were transferred to the planar surface of a ZrO₂ SIL and centered using a micromanipulator. These slabs were fabricated by inductively coupled plasma (ICP) reactive ion etching (RIE), using an initially 50 μm thick diamond sample. Fig. 24 a) shows a bright-field image of three slabs recorded through the SIL, where the interference colors indicate the presence of an air gap between diamond pieces and SIL. Slab (1) has a clear gradient in the gap size, being the smallest in the white corner and increasing with the colors orange, red, violet, blue, green etc. Constructive interference in the reflection occurs at gap sizes $d = \frac{(2n+1)\lambda}{4}$ with $n \in \mathbb{N}_0$. Supposedly, the first two colors correlate to a gap size of $d = \frac{\lambda}{4}$ and the subsequent colors, starting with the shortest visible wavelength of violet, to $d = \frac{3\lambda}{4}$. Therefore, the gap size in the white area is estimated to be at most 150 nm, which is a quarter of the yellow wavelength.

However, the fact that the white area is much brighter than the background (reflection only at ZrO₂-air interface) indicates that the contact is still not very good there. With a perfect contact, only the diamond-air interface would have a significant reflectivity, whereas a bad contact leads to the three reflecting interfaces ZrO₂-air, air-diamond and diamond air. The imperfect contact quality is not effectively improved by pressing the slab on the SIL. Therefore, it is likely caused by particle contamination on the slab, which possibly originated in the etching process or the preparation of SIL and diamond. The particles seemed to stick to the slabs since the interference colors didn't significantly change when moving the slabs laterally on the SIL surface. Slab (3) showed no interference colors indicating an air gap which is greater than the coherence length of the thermal light ($\sim 1 \mu\text{m}$) used for illumination.

Slabs (1) and (2) were rearranged to the center of the SIL and observed in the confocal scan in Fig. 24 b). Despite the high NV density in the CVD diamond, single NV centers can be resolved due to the SIL resolution enhancement and the small slab thickness. The NV center in the red circle is relatively isolated and yields $g^2(0) < 0.5$, a calculated saturation count rate of 250 ± 10 kcps and a saturation power of 217 ± 11 μW . Although the single NV center count rate is much higher than without ZrO_2 SIL, it is still somewhat reduced compared to our studies with a ZrO_2 SIL on polycrystalline bulk diamond (see Sect. 4.1.2). In combination with the higher saturation power, this confirms the existence of a sizeable air gap between diamond and SIL. Consistent with this observation is the fact that the NV centers in slab (2) are generally darker.

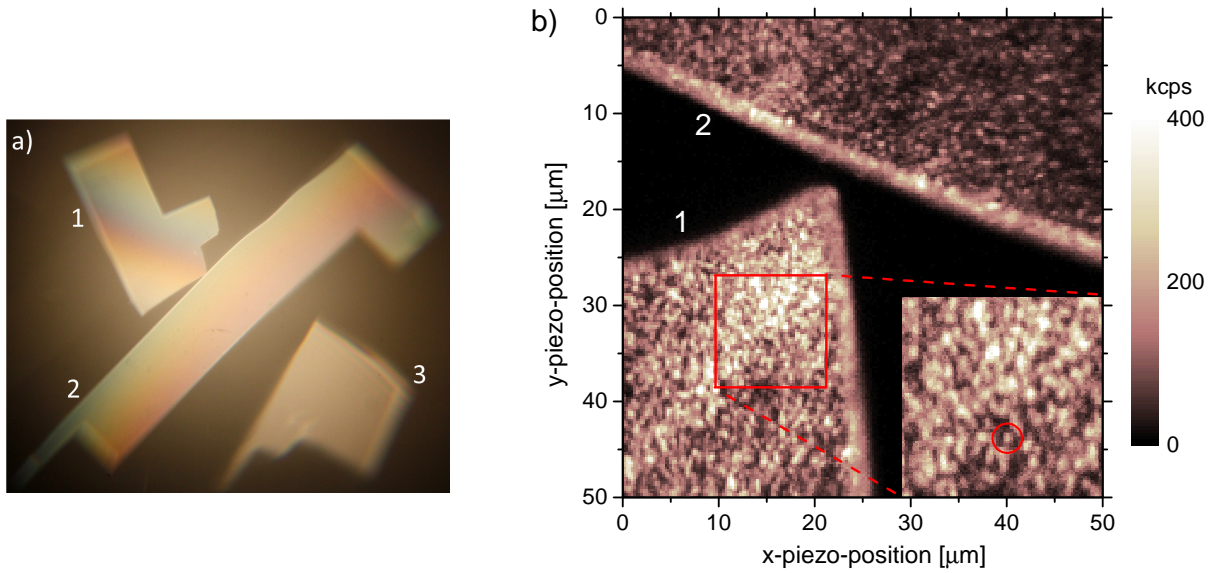


Fig. 24: **a)** Bright-field image of three thin CVD diamond slabs as seen through a ZrO_2 SIL. The brightness and the interference colors indicate an air gap between slab and SIL, where the white corner of slab (1) represents the smallest gap. Spherical aberration of the SIL is apparent in the edge of the image. **b)** Confocal scan of slabs of (1) and (2) at 800 μW excitation. The bright area in the bottom left represents the corner of slab (1) with the smaller air gap, where single NVs, such as the one indicated by the red circle, have saturation count rates of about 250 kcps. In slab (2), the NVs are generally darker, supposedly due to a larger air gap.

4.3.2 GaP SIL

The next step was to transfer the thin slabs from the ZrO_2 to the GaP SIL to realize a dielectric antenna with a much higher count rate. However, no usable results were obtained with these slabs on the GaP SILs, assumingly because of much too large gaps due to further contamination of the slabs. Better results were achieved with diamond cantilevers which are significantly smaller than the slabs and have dimensions of about $15 \mu\text{m} \times 3 \mu\text{m} \times 1.5 \mu\text{m}$. Similar to the slabs, the cantilevers were released and positioned on the SIL using a micromanipulator (Fig. 25 a)). The advantage of many small cantilevers over few larger slabs is that they are less likely to be polluted by particles and are therefore much more likely to sufficiently adhere to the SIL. The bright- and dark-field images in Fig. 25 b) and c) show which cantilevers have a good contact based on the criteria developed in the previous Sect.

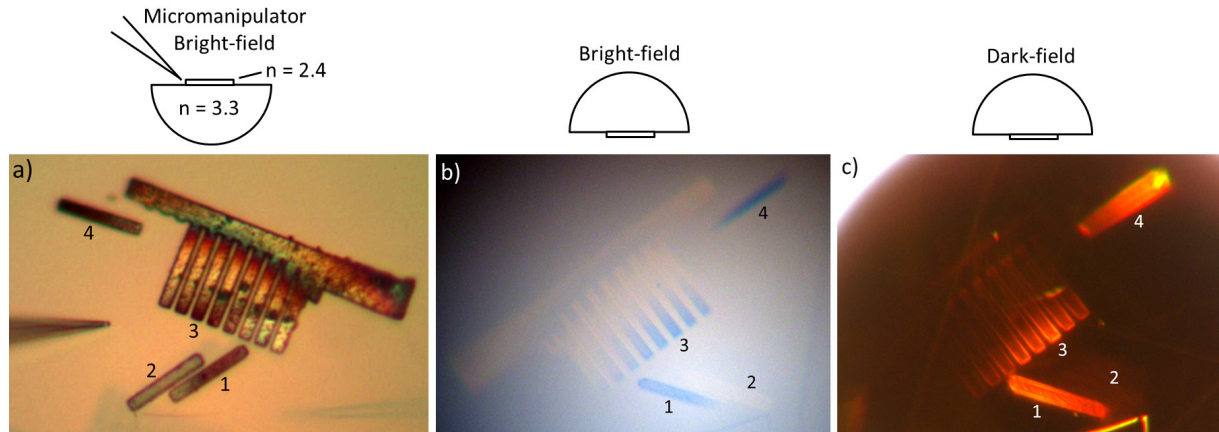


Fig. 25: **a)** Bright-field image of the cantilevers arranged around the center of the GaP SIL, which is located between cantilevers (1) and (2). The two single cantilevers (1) and (4) and the end of some connected cantilevers (3) are very dark due to the good contact to the GaP, acting like an anti-reflection coating with a refractive index between GaP and air. Cantilever (4) bonded so well to the SIL that it couldn't be moved laterally anymore. The needle of the micromanipulator is seen in the left of the image. **b)** Bright-field image through the SIL. Well contacted cantilevers (1,3,4) are again darker, while the badly contacted cantilever (2) is almost not recognized. **c)** Dark-field image through the SIL. Here, the good contacts are brighter because on the one hand more light from the microscope enters the cantilevers (no total internal reflection in GaP despite high angles) and on the other hand more of the light scattered in the cantilevers couples back into the SIL. Chromatic aberration is observed in cantilever (4).

As expected, more fluorescence is collected from the cantilevers with the best contacts (Fig. 26). Cantilevers (1) and (3) are much brighter than (2). However, single NV centers are not resolved, supposedly due to a too high density in the CVD diamond. Unfortunately, a high background fluorescence is present because the sample had not been properly cleaned, which makes it impossible to record reliable saturation curves.

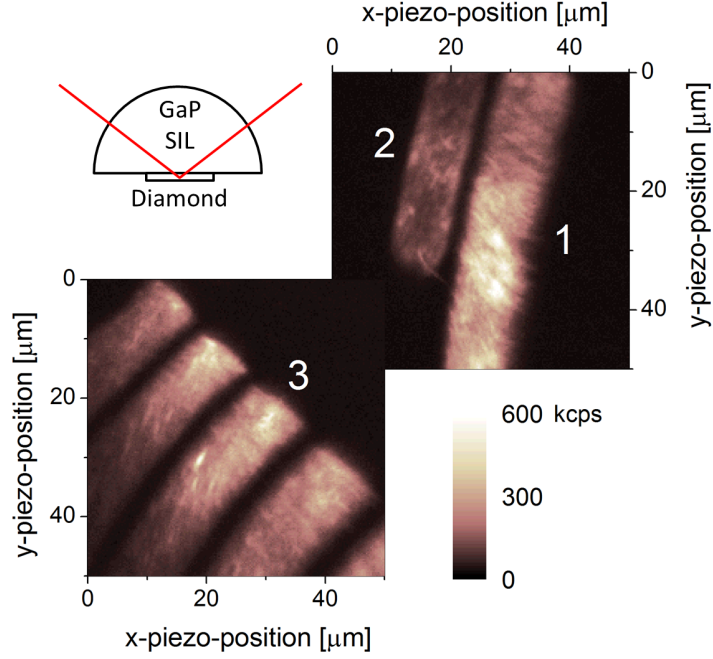


Fig. 26: Two contiguous scans of the cantilevers around the center of the GaP SIL at 435 μW with a multi-mode collection fiber. A large contrast between regions with good (1,3) and bad contact (2) is observable. ESR and $g^2(\tau)$ measurements suggest that the bright spots in the cantilevers are not single NV centers but possibly residues from the fabrication of the cantilevers (see also Fig. 29).

Most interestingly, when turning SIL and sample upside down (not looking through the SIL), the regions with good contact that yielded bright fluorescence when looking through the SIL were now much darker (Fig. 27 a)). This means that much of the fluorescence is drawn from the diamond into the higher-refractive-index GaP which is the basic principle of the dielectric antenna. Cantilever (1) was 2 to 3 times brighter through the GaP SIL whereas cantilever (2) was 10 times darker through the SIL at the same excitation power. However, this factor of 2 to 3 is very difficult to interpret due to the simultaneous change of excitation intensity and detection volume when using the SIL. A more accurate measurement would require observation at single NV fluorescence which was not possible with the present sample. Nevertheless, a well functioning dielectric antenna should deliver much higher count rates in the order of 1 Mcps for one single NV center. This discrepancy could be caused by a still imperfect contact quality possibly due to surface roughness, by emission angles larger than the collection angle of the objective or by defects of the GaP SIL. It is also not understood why the resolution with SIL is barely better than without SIL (Fig. 26 and 27 a)).

When using a single-mode collection fiber, the resolution is strongly increased and the count rate decreased due to a smaller collection volume (Fig. 27 b)). Many diffraction

limited spots become visible which look like extremely bright NV centers at first sight. But they don't show any saturation behaviour and the $g^2(\tau)$ and ESR measurements reveal no significant NV signatures. To confirm that some of the signal stems from NV centers, images with and without microwave field on resonance were recorded. The difference between these two images shows that NV center fluorescence is present, but not in the bright spots (Fig. 28). Therefore, the bright spots are assumed to be small fluorescent particles on the surface of the cantilevers (see Fig. 29). It is notable that the count rate from the well-contacted cantilever (1) through the SIL is about 8 times lower using a single-mode collection fiber than using a multi-mode fiber (image not shown). In contrast, from the other side (not through the SIL) the factor of multi-mode to single-mode is only about 3. Supposedly, larger angles are emitted into the GaP SIL, which is expected for dielectric antennas, lowering the coupling efficiency into the single-mode fiber (see Sect. 4.4).

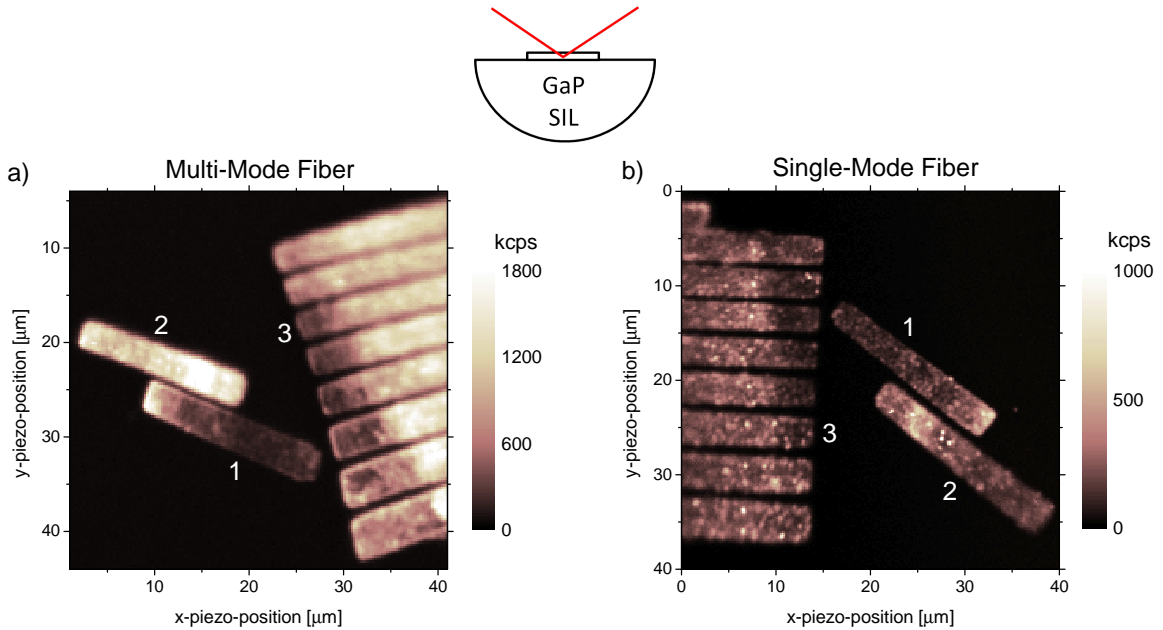


Fig. 27: a) Same cantilevers upside down, not through the GaP SIL, at $435 \mu\text{W}$ with a multi-mode collection fiber. Darker regions with good diamond-GaP contact indicate the dielectric antenna effect, where most of the fluorescence is drawn into the GaP. b) Same as a) but with a single-mode collection fiber and a different sample orientation. Many spots are observed with the better resolution, which don't represent single NV centers but supposedly residues on the surface.

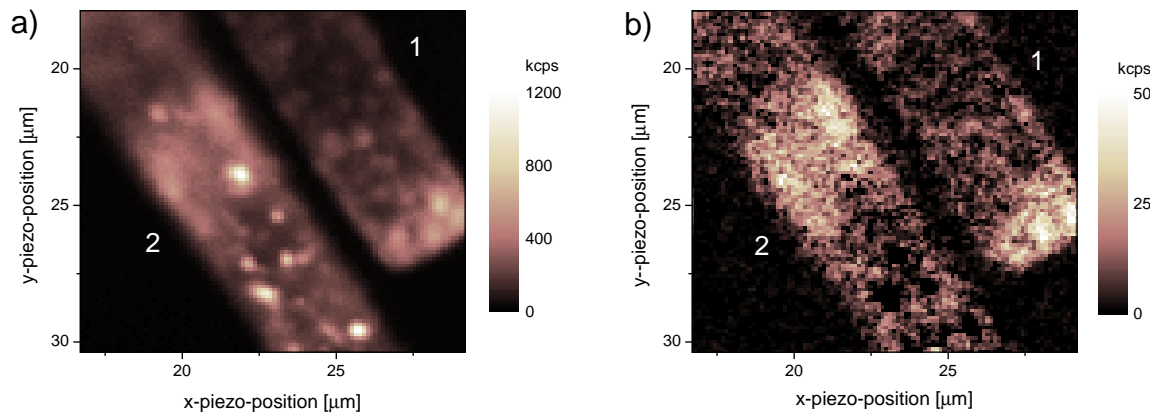


Fig. 28: **a)** Detailed scan of cantilevers (1) and (2) as in Fig. 27 b) using a single-mode fiber. **b)** Reduction of the count rate when switching on the microwave field on resonance at 2.87 GHz with the same field of view as a). NV fluorescence is revealed in broad regions rather than in located spots. The fact that the NV centers are not resolved individually is probably due to a high density. For some of the bright spots in a), even an increase of count rate with MW is observed. We assign this to a slight shift in focus towards the cantilever surface when turning on the MW due to a contact of the antenna with the SIL.

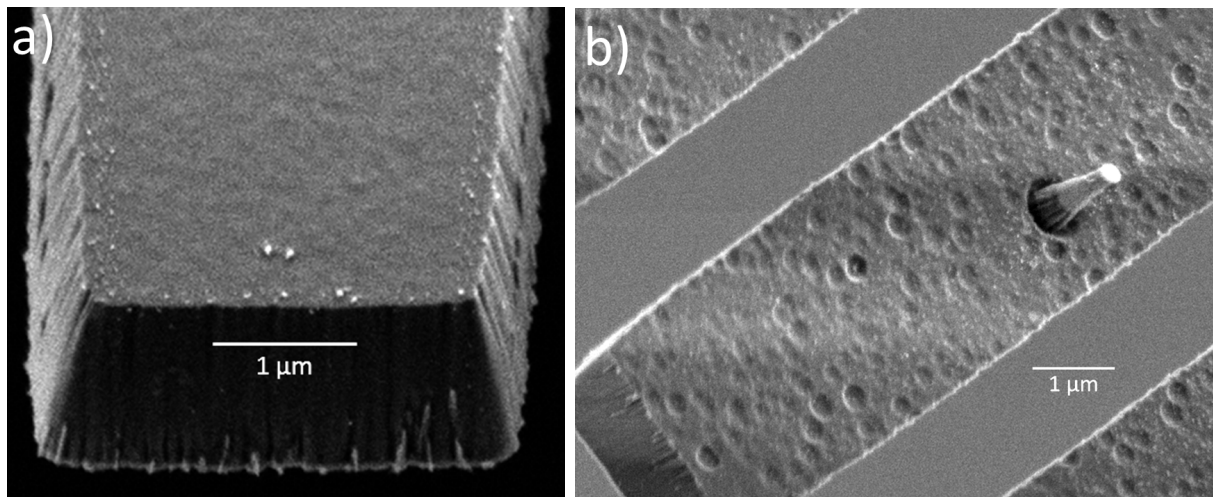


Fig. 29: Scanning electron microscope (SEM) images of cantilevers from the cantilever sample used above. **a)** The side of the cantilevers which was contacted to the GaP SIL. Especially at the edge, many residual particles from the etching process are found. These could limit the contact quality and therefore the count rate measured through the GaP SIL. **b)** The other side of the cantilevers is fully covered with dimples and small particles and some cantilevers are equipped with a nanowire. The particles on both sides of the cantilevers might cause the bright fluorescent spots seen in the scans.

4.4 Back Focal Plane Imaging

Back focal plane imaging allows to measure the angle of the collected fluorescence. This is particularly interesting in cases where the emission pattern carries specific signatures of the geometry of the sample. Besides a high NV center density bulk diamond, which yields a rather isotropic emission, we looked at a nanowire, a nanodiamond on a SIL, and our dielectric antenna. With the observed emission angles, we can estimate the performance of our sample or SIL and obtain information about the contact quality of the cantilevers on the GaP SIL.

Collecting from several μm inside a CVD diamond, a relatively uniform illumination of the objective is observed (bright filled circle in the inset in Fig. 30). The measured angular power density is compared to the one expected for an isotropic emission inside diamond, where the refraction at the surface lowers the intensity at higher angles (blue curve). This is derived as follows:

$$\sin(\theta_1) = n \sin(\theta_2) \quad \rightarrow \quad \frac{d\theta_2}{d\theta_1} = \frac{d \arcsin\left(\frac{\sin(\theta_1)}{n}\right)}{d\theta_1} = \frac{\cos(\theta_1)}{n\sqrt{1 - \left(\frac{\sin(\theta_1)}{n}\right)^2}} \quad (10)$$

where n is the refractive index of diamond and θ_1 and θ_2 the angle outside and inside diamond, respectively. A high density of NV centers with different orientations and two perpendicular dipole emissions each are assumed to be well approximated by an isotropic emission. However, the measured values are significantly lower than expected at high angles, which might be caused by higher losses inside the objective for off-axis beams. In the following, we will present our raw data (black) together with rescaled data-sets to correct for this possible collection reduction at high angles.

To additionally confirm the validity of our back focal plane imaging, we examined two diamond photonic nanostructures. A less homogeneous emission is observed with a CVD nanowire (Fig. 31 a). In the CCD image as well as in the graph, a relatively abrupt decrease of intensity is observable at $\theta \approx 30^\circ$. This decrease is in agreement with simulations by Hausmann et al. for a sum of perpendicular and parallel dipoles in a nanowire and confirms an exit NA of the nanowire of about 0.5 [39]. We note however that the signal for $\theta > 30^\circ$ is larger than expected. The large background at high angles could be caused by surface fluorescence or structural defects of the nanowire.

A ring structure is seen with a 100 nm diameter nanodiamond containing a single NV center on the flat surface of a ZrO₂ SIL (Fig. 31 b)). The strong NV emission beyond the

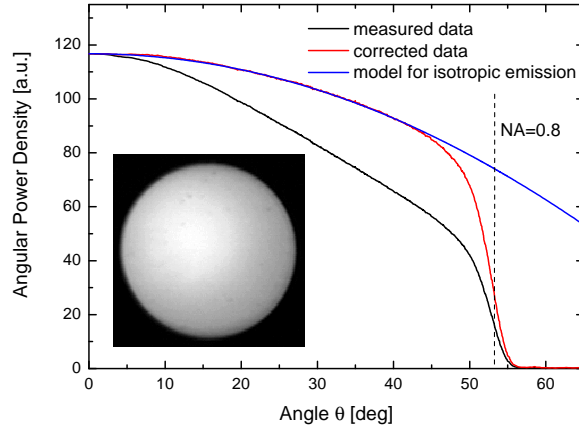


Fig. 30: Back focal plane image and analysis of the angular power density of the emission from a CVD diamond. The isotropic emission with refraction correction (Eq. 10) is seen as the blue curve. The red curve represents a 4th order polynomial correction of the black curve to fit to the expected homogeneous refraction compensating for possible losses at high angles.

critical angle at 27° ("forbidden light") indicates a very good contact, i.e. a distance of the nanodiamond to the ZrO_2 surface $z_0 \ll \lambda$. The maximum in the angular power density is found slightly outside of the critical angle which is comparable to the theoretical work of Lukosz for dipoles parallel to the surface [40]. Another reason for a shift to higher angles could be an effective refractive index larger than 1 in the nanodiamond leading to a larger critical angle.

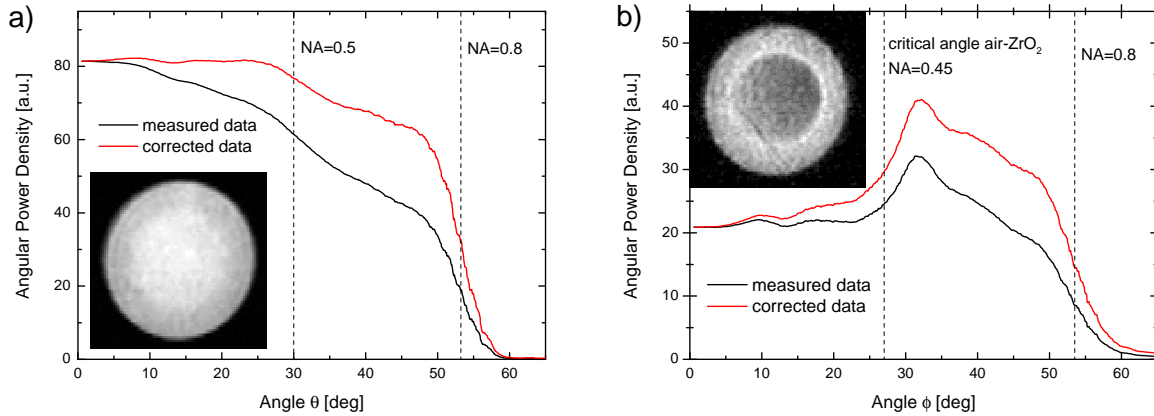


Fig. 31: Back focal plane image and analysis of **a)** a CVD nanowire, where the intensity significantly decreases after about 30° . **b)** a 100 nm diameter nanodiamond with a single NV center on a ZrO_2 SIL. The asymmetric intensity inside the ring possibly contains information about the orientation of the two NV dipoles.

When observing the bare GaP-air interface through a GaP SIL, a weak fluorescence is recorded. Its angular distribution again shows a ring structure with a maximum around 21° which is slightly above the critical angle for a GaP air interface of 18° (Fig. 32 a)).

This curve looks similar to the one calculated by Lukosz for randomly oriented parallel dipoles at a surface (Fig. 32 b)). However, dipoles perpendicular to the surface should cause a sharp peak exactly at the critical angle. Possibly, the peak is blurred by the finite angular resolution and not separable from the maximum of the parallel dipole emission. Additionally, the calculated angles might be inaccurate because of a distorted Fourier plane due to the objective which contains many different lenses.

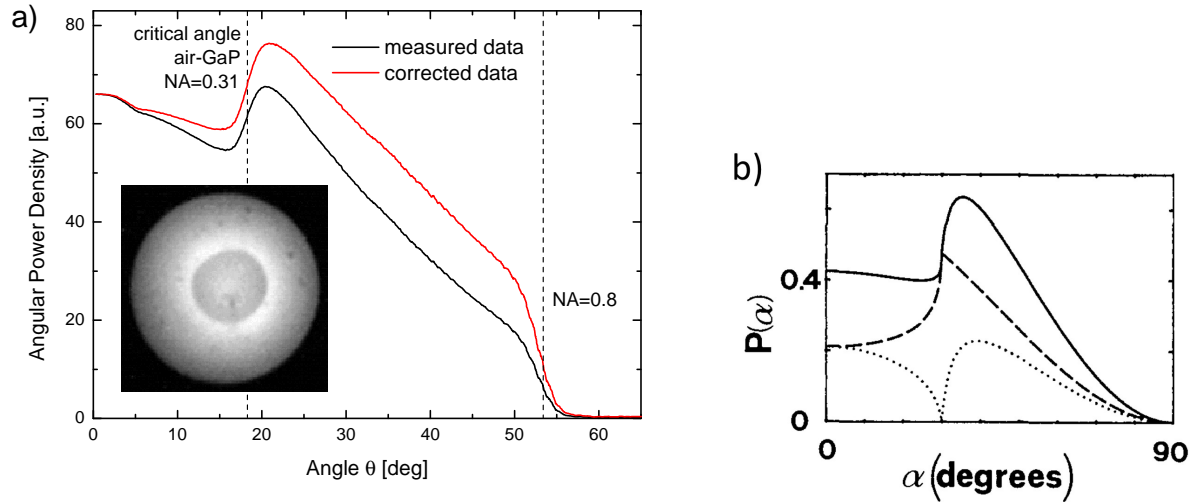


Fig. 32: a) Back focal plane image and analysis of the air-GaP interface through the GaP SIL, at $580 \mu\text{W}$ excitation and a CCD integration time equivalent of 26 s. A pronounced ring is observed slightly outside the critical angle ($\text{NA} = 0.31$) which is comparable to the calculation of Lukosz [40] presented in b). Here, the angular power density [a.u.] is plotted as a function of the emission angle for different orientations of parallel dipoles at a relative refractive index of $n = 2$. The dashed line is for s-polarized light, the dotted line for p-polarized light and the continuous line for the sum of both. The maximum of emission lies slightly above the critical angle (here 30°).

With our back focal plane imaging now fully established, we proceed by studying our dielectric antenna discussed in Sect. 4.3.2. Cantilever (1), which has a good contact to the GaP SIL, shows a relatively uniform emission over the whole angular range with slightly higher intensity at large angles (Fig. 33 a)). Emission beyond the critical angle of 47° ($\text{NA} = 0.74$) indicates that at least some of the emission originates from close vicinity of the interface to the SIL. In contrast, cantilever (2), having a bad contact to the SIL, emits only into small angles. This is because the light passes an air-GaP interface and is emitted only within the critical angle (Fig. 33 b)).

When removing the pinhole of our detection system (cf. Sect. 3.2, Fig. 11), the resolution of the back focal plane image increases and two peaks appear at very large angles in two opposite directions (Fig. 34). The peaks appear around the critical angle of a diamond-GaP interface as expected for a dielectric antenna (see Sect. 2.3). Interestingly, the radial directions, in which the peaks are observed, only depend on the orientation of the

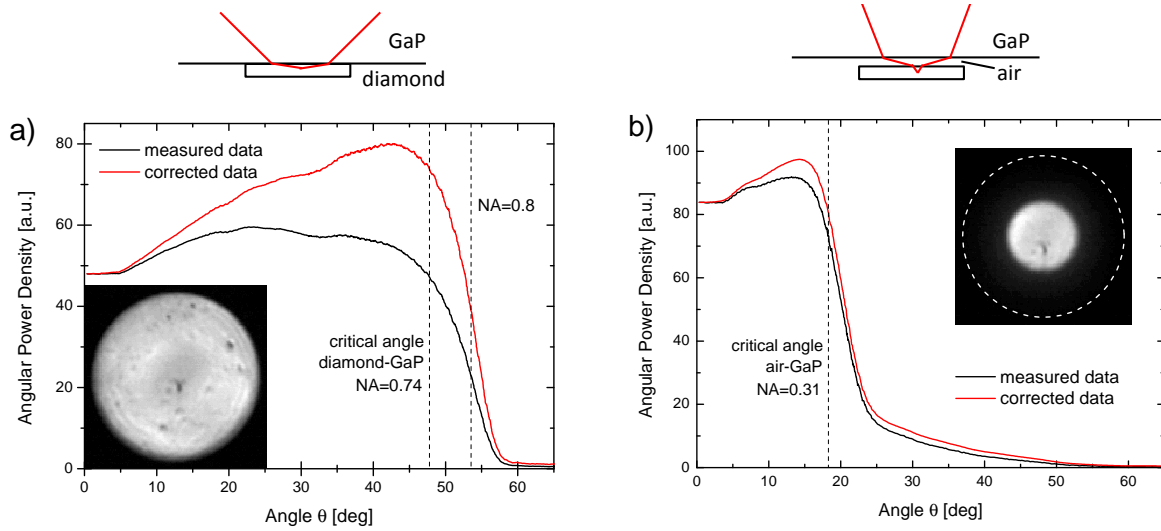


Fig. 33: Back focal plane image and analysis of the cantilever fluorescence with a GaP SIL with **a)** good contact, where the whole objective is illuminated and **b)** bad contact, where the collected light is more or less constricted to within the critical angle of the air-GaP interface. The white dashed circle indicates the objective aperture. Defects of the spherical surface of the SIL are imaged as dark spots in both back focal plane images. 580 μ W excitation power and 2.6 s integration time are used in both a) and b).

cantilever itself (Fig. 35 a)). Therefore, we conclude that for a dielectric antenna, the lateral dimensions of the middle layer needs to be larger than the current width of 3 μ m.

By imaging the cantilevers in real space, we observe that the fluorescence emerges not only from one point but rather an area of the cantilevers (Fig. 35). Supposedly, both excitation and fluorescence are slightly delocalized inside the laterally quasi-waveguiding cantilever which questions the use of a confocal setup if collection efficiency should be high. This could also explain why about 8 times more light was collected with the multi-mode fiber than with the single-mode fiber from the well contacted cantilever, apart from a less efficient coupling of large angles into the single-mode fiber. However, we assume that for a very well bonded piece of diamond with a completely clean and smooth surface, this delocalization of the emitted light would be significantly smaller.

Overall, the good contact quality of one of the cantilevers could be confirmed using the back focal plane imaging. However, since no single NV centers could be resolved in this sample and a large background fluorescence is present, little can be said about the effect of the NV center orientation on the angular emission.

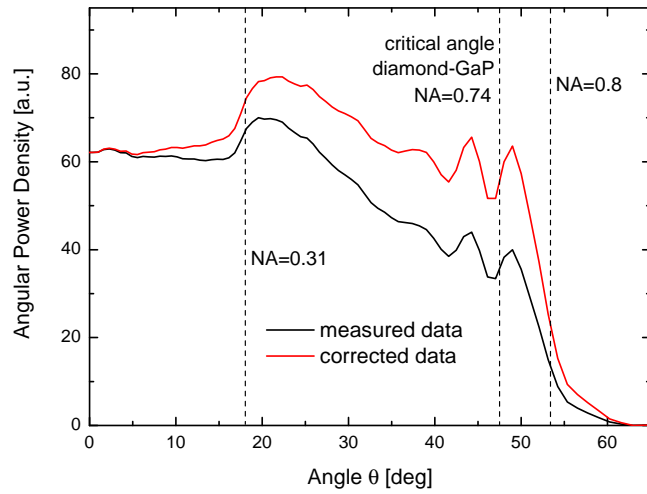
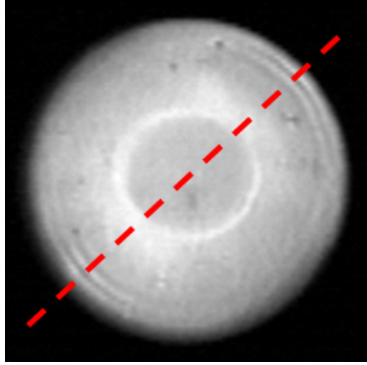


Fig. 34: Back focal plane image of the well-contacted cantilever as in fig. 33 a) but without pinhole. Apart from a superimposition with the background imaged in fig. 32, the increased resolution reveals large angle maxima in direction of the cantilever (red dashed line). The analysis of this region reveals that the peaks are around the critical angle of 47 degrees ($NA = 0.74$). The red curve is again corrected for possible objective losses. 580 μW excitation power and 1.3 s integration time is used.

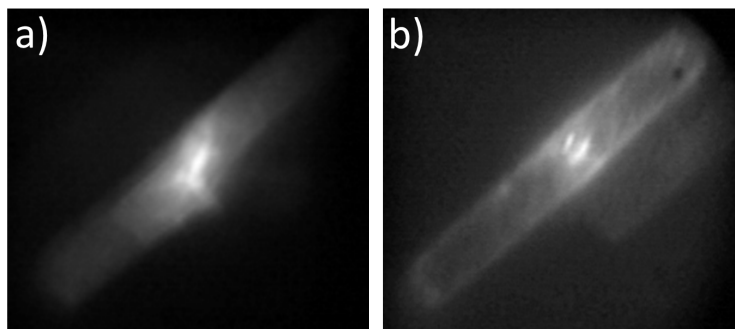


Fig. 35: CCD images of the same cantilevers as above with **a)** good contact and **b)** bad contact. Both show a fluorescence over an extended area. In **b)**, a significant part of the collected light travels until the edge of the cantilever and couples then into the SIL, which makes sense for a cantilever with better waveguide properties due to the air gap. Both are excited with 580 μW but **b)** has a 4 times longer integration time, confirming its smaller collection efficiency.

5 Summary and Outlook

We successfully increased the collection efficiency of single NV center fluorescence for both bulk diamond and thin diamond slabs by a factor of about 4 using a ZrO_2 SIL. Simultaneously, the signal-to-noise ratio was improved because of a smaller background due to a smaller detection volume. Good contact qualities between sample and SIL were demonstrated, where almost none of the laser light was reflected at the ZrO_2 -diamond interface. Although the resolution measurements were not fully conclusive because of the observed overshoots at the grating edges, the resolution enhancement is estimated to be around $n_{\text{ZrO}_2} = 2.2$. This was confirmed by the observation of a similar NV center spot size with and without SIL in terms of piezo movement, where magnification and resolution compensate each other.

With the GaP SIL, several additional challenges arose. One was that the 532 nm light is completely absorbed by GaP, which however could be solved by using a tunable laser at 560 nm. Another was the uneven surface of the GaP SIL which made good contacts to bulk diamonds impossible. In this case, always two separate lines with high reflectance, representing the GaP-air and air-diamond interfaces, could be observed. Therefore, it is not surprising that the measured count rates were not at all close to what would be expected theoretically with the high refractive index of $n_{\text{GaP}} = 3.3$. Rather, the obtained collection efficiency was similar with and without SIL. Other challenges were chromatic aberration in GaP, which can be compensated by changing the alignment of the excitation beam, and structural defects on the spherical surface of the SIL.

The problem with the contact quality of diamond and the GaP SIL should be solvable using thin diamond slabs which are flexible and also small in lateral dimensions. Thin slabs with thicknesses in the order of a μm in contact with a high refractive index material are also the key ingredients to realize coupling of NV centers to a dielectric antenna. Good contact of some diamond pieces (cantilevers) was observed through the low reflectivity in the bright-field microscope image and the same cantilevers yielded higher fluorescence count rates in the scans. Although the count rates were not as high as they should be in a well working dielectric antenna, the fact that from the other side (not through the SIL), exactly these cantilevers were darker proves that most of the fluorescence is redirected into the GaP. However, a lot of the light must be lost, possibly due to scattering, too large emission angles or a too small collection focus in case of a delocalized emission.

Moreover, the back focal plane images revealed useful information about the angular

distribution of the collected fluorescence and confirmed the very different contact quality of the two studied cantilevers via the measured emission angles. In the direction of the cantilever, peaks were observed around the critical angle which is typical for dielectric antennas. Therefore, although the cause for the low count rates could not be determined, it could be shown that, in general, the realization of a dielectric antenna with thin diamond slabs and a GaP SIL should be possible.

As a next step, the experiments should be repeated with cleaner cantilevers or thin slabs, where single NV centers are observable. Then it will be possible to determine the saturation count rates and investigate the influence of the NV orientation on the angular emission pattern in the back focal plane image. It may also be necessary to use GaP SILs with higher structural quality, if possible with smaller dimensions, allowing to use a higher NA objective with a smaller working distance. Further investigation should be done about how localized the emission enters the high index medium in a dielectric antenna to adjust collection spot size. Additionally, simulations could give new insights into optimal layer thickness, NV positions and necessary NA_{obj} .

Acknowledgments

I would very much like to thank the professors Patrick Maletinsky and Richard Warburton who made this project possible. Prof. Patrick Maletinsky carefully introduced me into the subject and took the time to explain me many issues in the lab and in theory. I am grateful for the steady support I got from the entire group of Prof. Patrick Maletinsky, especially for the help of Dr. Elke Neu, Dr. Jean Teissier, Dr. Marc Ganzhorn and Patrick Appel. I was also greatly supported by members of the group of Prof. Richard Warburton, especially from Timo Kaldewey with the GaP SIL experiments and Daniel Riedel with the dielectric antenna simulations. Additionally, I am grateful to the group of Prof. Martino Poggio for introducing me into their micromanipulator.

References

- [1] G. Davies and M. F. Hamer, “Optical studies of 1.945 eV vibronic band in diamond,” *Proceedings of the Royal Society of London Series A-mathematical and Physical Sciences*, vol. 348, p. 285, 1976.
- [2] A. Gruber, A. Drabenstedt, C. Tietz, L. Fleury, J. Wrachtrup, and C. von Borczyskowski, “Scanning confocal optical microscopy and magnetic resonance on single defect centers,” *Science*, vol. 276, p. 2012, 1997.
- [3] G. Balasubramanian, P. Neumann, D. Twitchen, M. Markham, R. Kolesov, N. Mizuochi, J. Isoya, J. Achard, J. Beck, J. Tissler, V. Jacques, P. R. Hemmer, F. Jelezko, and J. Wrachtrup, “Ultralong spin coherence time in isotopically engineered diamond,” *Nat Mater*, vol. 8, p. 383, 2009.
- [4] L. I. Childress, *Coherent manipulation of single quantum systems in the solid state*. PhD thesis, Harvard University, 2007.
- [5] J. Taylor, P. Cappellaro, L. Childress, L. Jiang, D. Budker, P. Hemmer, A. Yacoby, R. Walsworth, and M. Lukin, “High-sensitivity diamond magnetometer with nanoscale resolution,” *Nature Physics*, vol. 4, p. 810, 2008.
- [6] P. Maletinsky, S. Hong, M. Grinolds, B. Hausmann, M. Lukin, R. Walsworth, M. Loncar, and A. Yacoby, “A robust scanning diamond sensor for nanoscale imaging with single nitrogen-vacancy centres,” *Nature Nanotechnology*, vol. 7, p. 320, 2012.
- [7] M. W. Doherty, N. B. Manson, P. Delaney, F. Jelezko, J. Wrachtrup, and L. C. L. Hollenberg, “The nitrogen-vacancy colour centre in diamond,” *Physics Reports-review Section of Physics Letters*, vol. 528, p. 1, 2013.
- [8] A. Beveratos, R. Brouri, T. Gacoin, A. Villing, J. P. Poizat, and P. Grangier, “Single photon quantum cryptography,” *Physical Review Letters*, vol. 89, p. 187901, 2002.
- [9] S. Hong, M. S. Grinolds, L. M. Pham, D. Le Sage, L. Luan, R. L. Walsworth, and A. Yacoby, “Nanoscale magnetometry with NV centers in diamond,” *Mrs Bulletin*, vol. 38, p. 155, 2013.
- [10] A. Sipahigil, M. L. Goldman, E. Togan, Y. Chu, M. Markham, D. J. Twitchen, A. S. Zibrov, A. Kubanek, and M. D. Lukin, “Quantum interference of single photons

- from remote nitrogen-vacancy centers in diamond,” *Physical Review Letters*, vol. 108, p. 143601, 2012.
- [11] W. Pfaff, T. H. Taminiau, L. Robledo, H. Bernien, M. Markham, D. J. Twitchen, and R. Hanson, “Demonstration of entanglement-by-measurement of solid-state qubits,” *Nature Physics*, vol. 9, p. 29, 2013.
- [12] T. Babinec, B. Hausmann, M. Khan, Y. Zhang, J. Maze, P. Hemmer, and M. Loncar, “A diamond nanowire single-photon source,” *Nature Nanotechnology*, vol. 5, p. 195, 2010.
- [13] A. Beveratos, R. Brouri, T. Gacoin, J. Poizat, and P. Grangier, “Nonclassical radiation from diamond nanocrystals,” *Phys. Rev. A*, vol. 64, p. 61802, 2001.
- [14] C. Santori, P. E. Barclay, K. C. Fu, R. G. Beausoleil, S. Spillane, and M. Fisch, “Nanophotonics for quantum optics using nitrogen-vacancy centers in diamond,” *Nanotechnology*, vol. 21, p. 274008, 2010.
- [15] K. Koyama, M. Yoshita, M. Baba, T. Suemoto, and H. Akiyama, “High collection efficiency in fluorescence microscopy with a solid immersion lens,” *Applied Physics Letters*, vol. 75, p. 1667, 1999.
- [16] J. P. Hadden, J. P. Harrison, A. C. Stanley-Clarke, L. Marseglia, Y.-L. D. Ho, B. R. Patton, J. L. O’Brien, and J. G. Rarity, “Strongly enhanced photon collection from diamond defect centers under microfabricated integrated solid immersion lenses,” *Applied Physics Letters*, vol. 97, p. 241901, 2010.
- [17] P. Siyushev, F. Kaiser, V. Jacques, I. Gerhardt, S. Bischof, H. Fedder, J. Dodson, M. Markham, D. Twitchen, F. Jelezko, and J. Wrachtrup, “Monolithic diamond optics for single photon detection,” *Appl. Phys. Lett.*, vol. 97, p. 241902, 2010.
- [18] L. Luan, P. R. Sievert, B. Watkins, W. Mu, Z. Hong, and J. B. Ketterson, “Angular radiation pattern of electric dipoles embedded in a thin film in the vicinity of a dielectric half space,” *Applied Physics Letters*, vol. 89, p. 031119, 2006.
- [19] X.-W. Chen, S. Götzinger, and V. Sandoghdar, “99% efficiency in collecting photons from a single emitter,” *Opt. Lett.*, vol. 36, p. 3545, 2011.
- [20] K. Lee, X. Chen, H. Eghlidi, A. Renn, S. Gotzinger, and V. Sandoghdar, “A planar dielectric antenna for directional single-photon emission and near-unity collec-

- tion efficiency,” in *Lasers and Electro-Optics Europe (CLEO EUROPE/EQEC), 2011 Conference on and 12th European Quantum Electronics Conference*, 2011.
- [21] C. Bradac, T. Gaebel, and J. R. Rabeau, “Nitrogen-vacancy color centers in diamond: Properties, synthesis, and applications,” in *Optical Engineering of Diamond*, pp. 143–175, Wiley-VCH Verlag GmbH & Co. KGaA, 2013.
- [22] V. M. Acosta, A. Jarmola, E. Bauch, and D. Budker, “Optical properties of the nitrogen-vacancy singlet levels in diamond,” *Phys. Rev. B*, vol. 82, p. 201202, 2010.
- [23] H. Bernien, L. Childress, L. Robledo, M. Markham, D. Twitchen, and R. Hanson, “Two-photon quantum interference from separate nitrogen vacancy centers in diamond,” *Phys. Rev. Lett.*, vol. 108, p. 043604, 2012.
- [24] J. Walker, “Optical absorption and luminescence in diamond,” *Rep. Prog. Phys.*, vol. 42, p. 1605, 1979.
- [25] M. Frimmer, A. Mohtashami, and A. Femius Koenderink, “Nanomechanical method to gauge emission quantum yield applied to nitrogen-vacancy centers in nanodiamond,” *Applied Physics Letters*, vol. 102, p. 121105, 2013.
- [26] T. P. M. Alegre, C. Santori, G. Medeiros-Ribeiro, and R. G. Beausoleil, “Polarization-selective excitation of nitrogen vacancy centers in diamond,” *Phys. Rev. B*, vol. 76, p. 165205, 2007.
- [27] E. L. Hahn, “Spin echoes,” *Physical Review*, vol. 80, p. 580, 1950.
- [28] C. Sparrow, “On spectroscopic resolving power,” *Astrophys. J.*, vol. 44, p. 76, 1916.
- [29] K. A. Serrels, E. Ramsay, P. A. Dalgarno, B. Gerardot, J. O’Connor, R. H. Hadfield, R. Warburton, and D. Reid, “Solid immersion lens applications for nanophotonic devices,” *J Nanophotonics*, vol. 2, p. 021854, 2008.
- [30] S. M. Mansfield and G. S. Kino, “Solid immersion microscope,” *Applied Physics Letters*, vol. 57, p. 2615, 1990.
- [31] M. Yoshita, K. Koyama, Y. Hayamizu, M. Baba, and H. Akiyama, “Improved high collection efficiency in fluorescence microscopy with a weierstrass-sphere solid immersion lens,” *Japanese Journal of Applied Physics*, vol. 41, p. L858, 2002.

- [32] M. Born and E. Wolf, *Principles of Optics*. Cambridge University Press, 2002.
- [33] K. Beha, A. Batalov, N. B. Manson, R. Bratschitsch, and A. Leitenstorfer, “Optimum photoluminescence excitation and recharging cycle of single nitrogen-vacancy centers in ultrapure diamond,” *Phys. Rev. Lett.*, vol. 109, p. 097404, 2012.
- [34] J. M. Dishman and J. DiDomenico, M., “Optical absorption by impurities in p-type gallium phosphide,” *Phys. Rev. B*, vol. 6, p. 683, 1972.
- [35] P. Fröhlich, “Die gültigkeitsgrenze des geometrischen gesetzes der lichtbrechung,” *Ann. Phys.*, vol. 370, p. 577, 1921.
- [36] W. Lukosz and R. E. Kunz, “Light emission by magnetic and electric dipoles close to a plane dielectric interface. ii. radiation patterns of perpendicular oriented dipoles,” *J. Opt. Soc. Am.*, vol. 67, p. 1615, 1977.
- [37] M. A. Lieb, J. M. Zavislan, and L. Novotny, “Single-molecule orientations determined by direct emission pattern imaging,” *J. Opt. Soc. Am. B*, vol. 21, p. 1210, 2004.
- [38] J. W. Goodman, *Introduction to Fourier Optics*. Roberts and Company Publishers, 2005.
- [39] B. J. M. Hausmann, M. Khan, Y. N. Zhang, T. M. Babinec, K. Martinick, M. McCutcheon, P. R. Hemmer, and M. Loncar, “Fabrication of diamond nanowires for quantum information processing applications,” *Diamond and Related Materials*, vol. 19, p. 621, 2010.
- [40] W. Lukosz, “Light emission by magnetic and electric dipoles close to a plane dielectric interface. iii. radiation patterns of dipoles with arbitrary orientation,” *J. Opt. Soc. Am.*, vol. 69, p. 1495, 1979.

Appendix

Calculation of Collection Efficiencies

For a given collection angle θ_{os} (inside diamond), the collection efficiencies are calculated as follows. For a vertical dipole:

$$\eta_v = \frac{1}{4\pi} \int_0^{2\pi} d\phi \int_0^{\theta_{os}} \sin^2(\theta) d\theta = \frac{1}{2} \int_0^{\theta_{os}} \sin^3(\theta) d\theta \quad (11)$$

Since the horizontal dipole is not symmetric in ϕ , we take an average over ϕ and only integrate over θ to obtain the collection efficiency. The average over ϕ is just the average of the p-polarized (parallel to the plane) and the s-polarized (perpendicular to the plane) situation. The p-polarization contributes with $\cos^2(\theta)$ and the s-polarization with 1. Therefore the collection efficiency for a horizontal dipole is

$$\eta_v = \frac{1}{2} \int_0^{\theta_{os}} \frac{\cos^2(\theta) + 1}{2} \sin(\theta) d\theta \quad (12)$$

Since the NV center has two perpendicular dipoles, the calculated collection efficiencies for the NV center provided in Table 1 are the averages of a vertical and a horizontal dipole or of two horizontal dipoles as derived here.

```
(* Mathematica code for simulation
of emission angles in dielectric antenna *)
```

```
(* 3 layer system
```

```
n1      Glass
```

```
n2      Diamond
```

```
n3      Gallium Phosphide
```

```
*)
```

```
(*Snell's law: angle of refraction  $\theta_j$  for a incident
light ray under angle  $\theta_i$  passing from layer i to layer j*)
```

```
 $\theta_j[ni\_ , nj\_ , \theta_i\_ ] := \text{ArcSin}\left[\frac{ni}{nj} \text{Sin}[\theta_i]\right];$ 
```

```
(* Fresnel-Coefficients rsij, tsij from layer j to layer i *)
```

```
 $rsij[\theta_i\_ , ni\_ , nj\_ ] = \frac{ni \text{Cos}[\theta_i] - nj \text{Cos}[\theta_j[\theta_i, ni, nj]]}{ni \text{Cos}[\theta_i] + nj \text{Cos}[\theta_j[\theta_i, ni, nj]]};$ 
```

```
 $tsij[\theta_i\_ , ni\_ , nj\_ ] = \frac{2 * ni \text{Cos}[\theta_i]}{ni \text{Cos}[\theta_i] + nj \text{Cos}[\theta_j[\theta_i, ni, nj]]};$ 
```

```
 $rpij[\theta_i\_ , ni\_ , nj\_ ] = \frac{+nj \text{Cos}[\theta_i] - ni \text{Cos}[\theta_j[\theta_i, ni, nj]]}{ni \text{Cos}[\theta_j[\theta_i, ni, nj]] + nj \text{Cos}[\theta_i]};$ 
```

```
 $tpij[\theta_i\_ , ni\_ , nj\_ ] = \frac{2 * ni \text{Cos}[\theta_i]}{ni \text{Cos}[\theta_j[\theta_i, ni, nj]] + nj \text{Cos}[\theta_i]};$ 
```

```

rs12 := rsij[θ1, n1, n2]
ts12 := tsij[θ1, n1, n2]
rp12 := rpij[θ1, n1, n2]
tp12 := tpij[θ1, n1, n2]
rs23 := rsij[θj[n1, n2, θ1], n2, n3]
ts23 := tsij[θj[n1, n2, θ1], n2, n3]
rp23 := rpij[θj[n1, n2, θ1], n2, n3]
tp23 := tpij[θj[n1, n2, θ1], n2, n3]
rs32 := rsij[θ3, n3, n2]
ts32 := tsij[θ3, n3, n2]
rp32 := rpij[θ3, n3, n2]
tp32 := tpij[θ3, n3, n2]
rs21 := rsij[θj[n3, n2, θ3], n2, n1]
ts21 := tsij[θj[n3, n2, θ3], n2, n1]
rp21 := rpij[θj[n3, n2, θ3], n2, n1]
tp21 := tpij[θj[n3, n2, θ3], n2, n1]

(* Lorentz reciprocity theorem →
Resulting electric field at position z for a thickness of l2 for layer 2
for a incoming wave propagating from infinity from the air/lens side
moving forward(p)/backward(m) having polarization p/s → "Eairps" *)

Elensps[θ3_, n1_, n2_, n3_, l2_, k_, z_] = - (Exp[i * n2 * k * Cos[θj[n3, n2, θ3]] *
z] * (-1 + rs32^2)) /
((1 + Exp[2 * i * n2 * k * Cos[θj[n3, n2, θ3]] * l2] * rs21 * rs32) * ts32);

Elensms[θ3_, n1_, n2_, n3_, l2_, k_, z_] =
(Exp[i * n2 * k * Cos[θj[n3, n2, θ3]] * (l2 - z)] * (-1 + rs32^2))
rs21 / ((1 + Exp[2 * i * n2 * k * Cos[θj[n3, n2, θ3]] * l2] * rs21 * rs32) * ts32);

Elensp[θ3_, n1_, n2_, n3_, l2_, k_, z_] = - (Exp[i * n2 * k * Cos[θj[n3, n2, θ3]] *
z] * (-1 + rp32^2)) /
((1 + Exp[2 * i * n2 * k * Cos[θj[n3, n2, θ3]] * l2] * rp21 * rp32) * tp32);

Elensmp[θ3_, n1_, n2_, n3_, l2_, k_, z_] =
(Exp[i * n2 * k * Cos[θj[n3, n2, θ3]] * (l2 - z)] * (-1 + rp32^2))
rp21 / ((1 + Exp[2 * i * n2 * k * Cos[θj[n3, n2, θ3]] * l2] * rp21 * rp32) * tp32);

```

(* Radiation pattern for a dipole at position z in layer 2 (n2) with thickness l2 in the direction of air(n1)/lens(n3) for a dipole parallel(p)/orthogonal(o) to the surface in polarization s/p. There is no s polarization for an orthogonal dipole → forbidden by geometry*)

$$\text{Plensps}[\theta_3, n1, n2, n3, l2, k, z] = \frac{3}{8\pi} * n3 * \text{Abs}[\text{Elensps}[\theta_3, n1, n2, n3, l2, k, z] + \text{Elensms}[\theta_3, n1, n2, n3, l2, k, z]]^2;$$

$$\text{Plenspp}[\theta_3, n1, n2, n3, l2, k, z] = \frac{3}{8\pi} * n3 * \text{Abs}[\text{Elenspp}[\theta_3, n1, n2, n3, l2, k, z] - \text{Elensmp}[\theta_3, n1, n2, n3, l2, k, z]]^2 * \text{Abs}[\text{Cos}[\theta_j[n3, n2, \theta_3]]]^2;$$

$$\text{Plensop}[\theta_3, n1, n2, n3, l2, k, z] = \frac{3}{8\pi} * n3 * \text{Abs}[\text{Elenspp}[\theta_3, n1, n2, n3, l2, k, z] + \text{Elensmp}[\theta_3, n1, n2, n3, l2, k, z]]^2 * \text{Abs}[\text{Sin}[\theta_j[n3, n2, \theta_3]]]^2;$$

(* Back Focal Plane Imaging - for explanation see theory Sect. 2.4 *)

$$\text{Plensp}[x, y] = \left(\text{Plensps}\left[\text{ArcSin}[\text{Sqrt}[x^2 + y^2]], 1, 2.41178, 3.27, \frac{1000 * 10^{-9}}{1}, \frac{2\pi}{637 * 10^{-9}}\right], \frac{500 * 10^{-9}}{1} \right) * \text{Sin}[\text{ArcTan}[y/x]]^2 + \left(\text{Plenspp}\left[\text{ArcSin}[\text{Sqrt}[x^2 + y^2]], 1, 2.41178, 3.27, \frac{1000 * 10^{-9}}{1}, \frac{2\pi}{637 * 10^{-9}}\right], \frac{500 * 10^{-9}}{1} \right) * \text{Cos}[\text{ArcTan}[y/x]]^2 \Big/ \text{Cos}[\text{Sqrt}[x^2 + y^2]];$$

$$\text{Plenso}[x, y] = \text{Plensop}\left[\text{ArcSin}[\text{Sqrt}[x^2 + y^2]], 1, 2.41178, 3.27, \frac{1000 * 10^{-9}}{1}, \frac{2\pi}{637 * 10^{-9}}\right], \frac{500 * 10^{-9}}{1} \Big/ \text{Cos}[\text{Sqrt}[x^2 + y^2]];$$

(* These Contour Plots reproduce the simulated back focal plane images shown in Fig. 9. *)

```
ContourPlot[Plensp[x, y], {x, -0.8, 0.8}, {y, -0.8, 0.8},
  Contours → {Automatic, 200}, PlotLegends → Automatic, PlotRange → {0, 1.7},
  ContourStyle → None, ColorFunction → "GrayTones", PlotPoints → 60]
```

```
ContourPlot[Plenso[x, y], {x, -0.8, 0.8}, {y, -0.8, 0.8},
  Contours → {Automatic, 100}, PlotLegends → Automatic, PlotRange → {0, 3.5},
  ContourStyle → None, ColorFunction → "GrayTones", PlotPoints → 60]
```

Erklärung zur wissenschaftlichen Redlichkeit
(beinhaltet Erklärung zu Plagiat und Betrug)

~~Bachelorarbeit~~ / Masterarbeit (nicht Zutreffendes bitte streichen)

Titel der Arbeit (Druckschrift):

Enhancing Collection Efficiency of
Nitrogen Vacancy Fluorescence in Diamond
Using a Solid Immersion Lens

Name, Vorname (Druckschrift): Rohner Dominik

Matrikelnummer: 08-050-817

Hiermit erkläre ich, dass mir bei der Abfassung dieser Arbeit nur die darin angegebene Hilfe zuteil wurde und dass ich sie nur mit den in der Arbeit angegebenen Hilfsmitteln verfasst habe.

Ich habe sämtliche verwendeten Quellen erwähnt und gemäss anerkannten wissenschaftlichen Regeln zitiert.

Diese Erklärung wird ergänzt durch eine separat abgeschlossene Vereinbarung bezüglich der Veröffentlichung oder öffentlichen Zugänglichkeit dieser Arbeit.

ja nein

Ort, Datum: 20.11.2013

Unterschrift: 

Dieses Blatt ist in die Bachelor-, resp. Masterarbeit einzufügen.